Noise Prediction of Ducted Fans using Immersed Boundary Wall-Modeled Large Eddy Simulations

Aditya S. Ghate*, Man Long Wong, Gaetan K. W. Kenway, Jordan B. Angel, Eren Kiris, and Cetin C. Kiris
Volcano Platforms Inc., 422 Portage Ave, Palo Alto, CA 94306, USA

Full-annulus wall-modeled large eddy simulations (WMLES) of NASA's Source Diagnostic Test (SDT) are conducted using Volcano ScaLES for two geometries and three operating conditions to investigate fan noise propagation. Grid sensitivity studies isolate three factors: (i) near-wall rotor blade resolution, (ii) off-body resolution in vortical regions (shear layers and wakes), and (iii) resolution in irrotational but acoustically active regions. The results indicate that aerodynamic and aeroacoustic predictions impose different, sometimes competing, grid requirements. Practical grid design strategies for ducted fan simulations are proposed. The approach leverages the non-modeled quadrupole contribution in the porous Ffowcs Williams and Hawkings (FWH) formulation to guide consistent design of volumetric grids and porous FWH integration surfaces. Across all configurations and operating conditions, approximately 1 Billion-cell grids yield excellent agreement with experiments, with errors below 5 dB/Hz over the 1–20 kHz frequency range. For takeoff conditions with supersonic blade tip speeds, the simulations capture buzz-saw harmonics (multiple discrete tones). Random blade-to-blade staggering is introduced to emulate manufacturing variability. All simulations are completed on a single node (8× Nvidia L40S GPUs) in approximately 12–16 hours of wall-clock time, demonstrating strong potential for industrial application.

I. Introduction

The substantial reduction in aircraft noise since the introduction of high-bypass turbofan engines in the 1970s has been driven largely by decreases in jet exhaust noise associated with increasing bypass ratios. As propulsion systems evolve toward ultra-high bypass ratio (UHBR) architectures—with larger fan diameters, shorter nacelles, and fewer, more highly loaded turbine stages—turbomachinery noise has emerged as a critical contributor to overall aircraft noise. In particular, fan noise is projected to become the dominant source within the forward arc under most operating conditions [1]. This shift is accompanied by increased broadband and tonal content at higher, more perceptually sensitive frequencies due to reduced stage-to-stage acoustic filtering [2], leading to what has been described as a "turbine noise storm" [3].

Accurate prediction of these noise sources requires resolving flow physics spanning a wide range of spatial and temporal scales. Advances in high-fidelity, turbulence-resolving computational methods, particularly large eddy simulation (LES), have made such analyses increasingly tractable. Recent studies [4–8] demonstrate the growing capability of LES to capture broadband noise in ducted fan configurations. More recently, Brès et al. (2025) [9] and Sinha et al. (2023) [10] have applied scale-resolving simulations to proprietary turbofan configurations (multi-stage rotors with a modeled core section) using commercial CFD solvers with encouraging results, further highlighting the potential of such approaches for industrial aeroacoustic applications.

In this study, we consider the ducted fan tested in the early 2000s at NASA Glenn Research Center as part of the Source Diagnostic Test (SDT) experiments [11]. A newly developed immersed boundary, wall-modeled large eddy simulation code, Volcano ScaLES, is utilized. Several key questions are addressed as part of solver validation:

1) The ability to capture **blade-passing frequency (BPF) tones across a range of tip Mach numbers.** It is well known that certain BPF modes that are cut off at subsonic tip speeds (low revolutions per minute (RPM)) [12] become propagative at higher, transonic and supersonic tip speeds [13], thereby contributing to the far-field acoustic signature. Accordingly, three operating conditions are considered: a) approach (61.7% design speed), b) cutback (87.5% design speed), and c) takeoff (100% design speed). In addition to tonal noise, the simulations are evaluated for their ability to predict **broadband noise generated by multiple mechanisms** (e.g., rotor-stator interactions, rotor trailing-edge self-noise, and interactions between the cowl boundary layer and blade tips).

*Corresponding author.

2) The ability of simulations to capture the **sensitivity of propagated noise to outlet guide vane (OGV) configuration**. Since rotor wake-OGV interactions are a dominant source of downstream-propagated noise, this sensitivity is assessed across all three operating conditions. Two OGV configurations are considered: a) a baseline configuration with 54 smaller, unswept vanes, and b) a low-noise configuration with fewer (26), swept vanes of larger chord, designed to maintain comparable aerodynamic performance.
3) The ability of simulations to reproduce the **low-frequency multiple pure tones (MPT) associated with the shaft frequency and its harmonics**. At high RPMs corresponding to takeoff conditions, the transonic flow near the blade tips leads to a strong upstream-propagating shock that is highly sensitive to small blade geometry variations [14, 15], resulting in the *buzz-saw* phenomenon. Following previous studies [6, 16, 17], this effect is emulated by introducing random blade-to-blade staggering.
4) **Optimal use of grid resolution**. While established guidelines exist for LES resolution in shear layers, boundary layers (attached and separated), and numerical discretization requirements for resolving acoustic waves, the coupled nature of hybrid computational fluid dynamics/computational aeroacoustics (CFD/CAA) approaches introduce additional considerations. In particular, when LES is used to resolve flow-generated sources and an acoustic analogy, e.g., the FWH method in the present work, is used for propagation, two key questions arise: a) where should the FWH integration surface be placed, and b) how should grid resolution be distributed within this region to efficiently capture all relevant noise sources? A significant portion of this work is dedicated to addressing these questions, including the distinction between resolution requirements for aerodynamic performance prediction and for accurate FWH-based acoustic propagation.

The SDT geometry is shown in Fig. 1 for the two OGV configurations. Table 1 summarizes the three operating conditions considered. All simulations performed used external flow, far-field conditions with a Mach 0.1 freestream consistent with the wind-tunnel conditions.

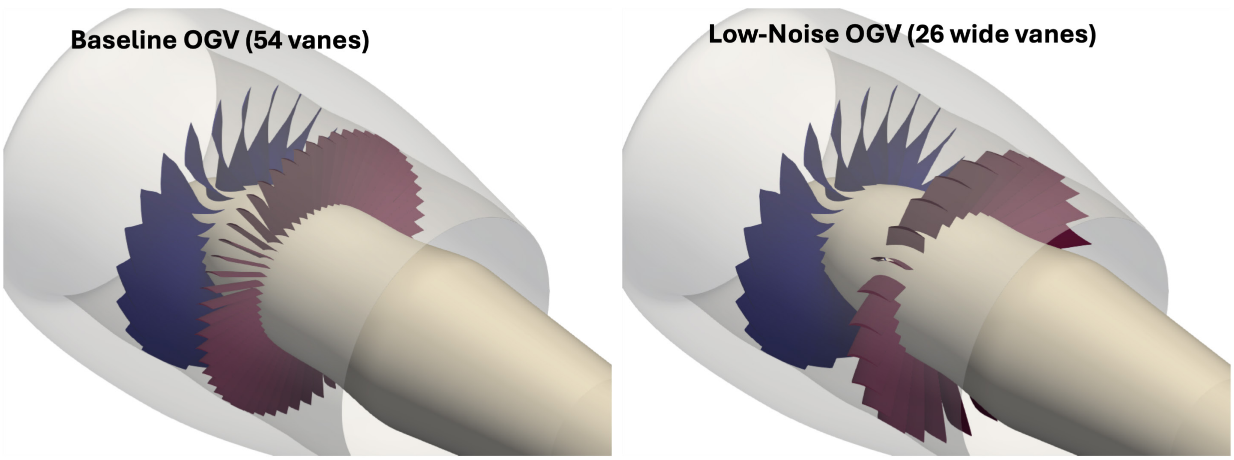

Fig. 1 Two geometric configurations of outlet guide vanes (OGVs) used in this study.

Table 1 The three distinct operating conditions simulated.

Condition	RPM	Design Speed	Rotor Tip Mach Number
Approach	7808	61.7%	0.669
Cutback	11075	87.5%	0.949
Takeoff	12657	100%	1.085

The remainder of the paper is organized as follows. Section II provides an overview of the numerical solver and a brief description of the FWH acoustic propagation methodology. Section III presents results for the three operating conditions and two OGV configurations, with emphasis on near-wall grid resolution requirements. Section IV examines the role of FWH endcap averaging in addressing missing quadrupole contributions and explores approaches for separating upstream and downstream acoustic components through appropriate partitioning of the FWH surface. Section V investigates the buzz-saw phenomenon, including the impact of under-resolved geometry associated with immersed boundary methods. Section VI revisits grid resolution, focusing on off-body resolution and its influence on FWH-propagated acoustics. Finally, Section VII summarizes the key findings and discusses practical considerations for applying LES to predict low-frequency content using narrow-band (low Δf) processing for spectra.

II. Volcano ScaLES

All simulations in this work are conducted with a GPU-accelerated numerical solver, Volcano ScaLES, with the compressible Navier–Stokes formulation using a nominally fourth-order accurate finite-difference spatial discretization of the convective fluxes with favorable kinetic energy and entropy consistency properties in turbulent regions, and the viscous flux discretization utilizes a mix of fourth and second order discretizations with improved resolution for high Reynolds number turbulent flows. The subgrid-scale stress tensor is modeled with the Smagorinsky model using the dynamic procedure [18, 19]. With the third-order strong stability preserving (SSP) Runge–Kutta (RK) time stepping method [20, 21], the overall numerical formulation is robust and has low dissipation and high isotropy, making it suitable for LES over a vast range of flow regimes with turbulence and acoustic wave radiation. For applications with discontinuities such as shock waves, a shock-capturing method with physics-based discontinuity sensors can be turned on to improve the robustness while the numerical dissipation is highly localized in regions with discontinuities. To handle complex geometries at high Reynolds numbers, an algebraic wall model is used in conjunction with an immersed boundary method that is highly robust for under-resolved thin features, small cavities, sharp edges/corners, etc. Two capabilities are provided to simulate rotating geometries. The first one is the sliding mesh capability, in which independently meshed rotating and stationary subdomains are coupled through time-accurate non-conformal interfaces that slide relative to one another. Another capability is the rotating wall boundary conditions, where the wall velocity at rotating surfaces is set to match the local rotational speed. While the first capability can be used for any rotating geometry, the rotating wall boundary conditions are only suitable for smooth and axisymmetric surfaces.

An in-situ acoustic solver, based on the FWH formulation, is developed and coupled with the GPU-accelerated CFD solver such that acoustics at off-body microphones can be computed on-the-fly during the simulations using near-field CFD data sampled on acoustic surfaces for subsonic flows, without requiring a large off-body grid to resolve the acoustic wave propagation from near-field to the microphones. The in-situ permeable FWH solver with WMLES is validated for noise generated from jets [22], a small quadrotor [23], and counter-rotating open rotors [24]. Note that the formulation ignores quadrupole contributions to propagated noise, and as such correction methods such as endcap averaging need to be utilized when appropriate [25, 26]. ScaLES has also been validated on a wide variety of CFD applications [27–33].

A unique aspect of the GPU solver, compared to other CFD codes, is that most of the work is compute-bound, so that high performance is achieved even on graphics-oriented, bandwidth-restricted devices, such as NVIDIA RTX 4090 and L40S GPU cards, which are far less expensive than higher memory bandwidth hardware, and make WMLES practical for use in an industrial setting. The combination of Cartesian methods and an explicit time stepping scheme yields extremely low memory requirements. For example, ScaLES can simulate around 6-7 million cells per GB of GPU memory depending on the complexity of the configuration. Simulations containing over 300 million cells are routinely performed on desktop computers containing just two NVIDIA RTX 4090 GPUs with 24 GB of memory each.

III. Role of near-wall grid resolution

The primary geometric resolution constraint for the SDT geometry is due to the 0.5 mm gap between the fan and the inner-walls of the nacelle. This imposes a minimum grid spacing restriction of approximately 0.25-0.5 mm to capture the pressure equilibration through the gap with sufficient numerical resolution. However, additional resolution requirements are certainly possible to capture the transitional turbulent boundary layers on the rotor and OGV blades. These considerations led to the three distinct grids that were utilized in this study as shown in Fig. 2. The total simulation cost is also included in Fig. 3 for the takeoff and the approach conditions representing the two extrema of the operation envelope simulated.

We begin the discussion of the preliminary results by examining power level (PWL) comparisons across operating conditions and OGV configurations relative to experimental measurements. The PWL in the simulations is computed using a linear microphone array [11], consistent with the experimental setup. These comparisons are shown in Fig. 4 through 11. Aerodynamic performance quantified using the measured mass-flow rate as well as the stagnation pressure and temperature ratios obtained at the nozzle exit are provided in Fig. 12. Several key observations are noted:

1) For the baseline OGV configuration at the takeoff condition, all three grid resolutions show good agreement with the experimental data. The first two BPF tones are captured within 2-3 dB, while the broadband spectra

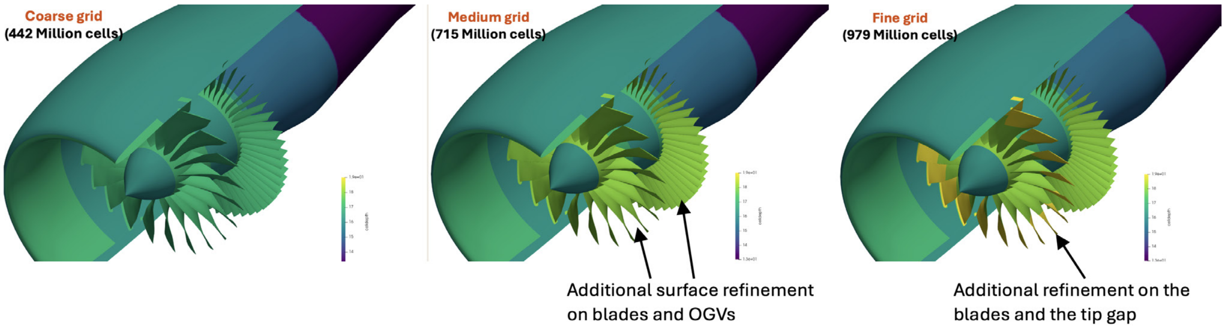

Fig. 2 Three mesh resolutions showing changes to the grid topology. Volume/off-body grid refinements are not changed between the three grids.

Case	Grid	# timesteps per rev	Walltime using 8x L40S GPUs for 10 revs
Take-off	Coarse (442M, 0.46mm)	21,000	5.6hrs
	Medium (715M, 0.23mm)	29,000	12.1hrs
	Fine (979M, 0.115mm)	58,000	36.6hrs
Approach	Coarse (442M, 0.46mm)	24,000	6.3hrs
	Medium (715M, 0.23mm)	39,000	17.5hrs
	Fine (979M, 0.115mm)	82,000	51hrs

Fig. 3 Computational cost of simulations at two operating conditions – approach and takeoff.

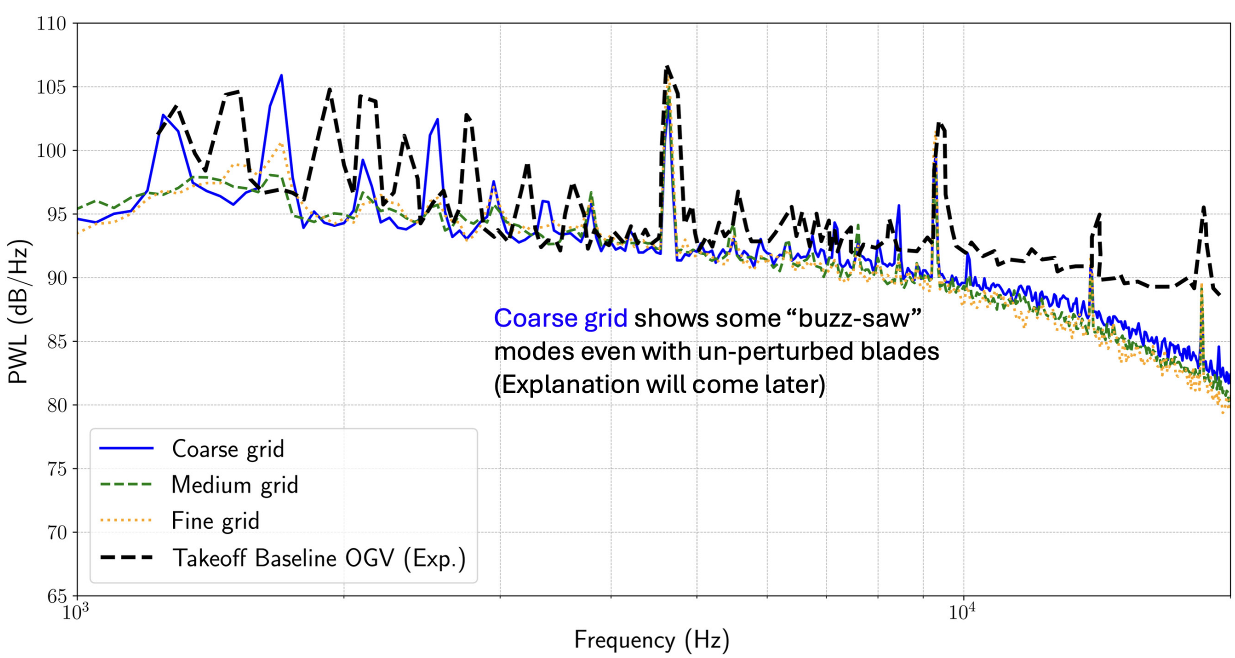

Fig. 4 PWL computed for the baseline OGV configuration at takeoff conditions.

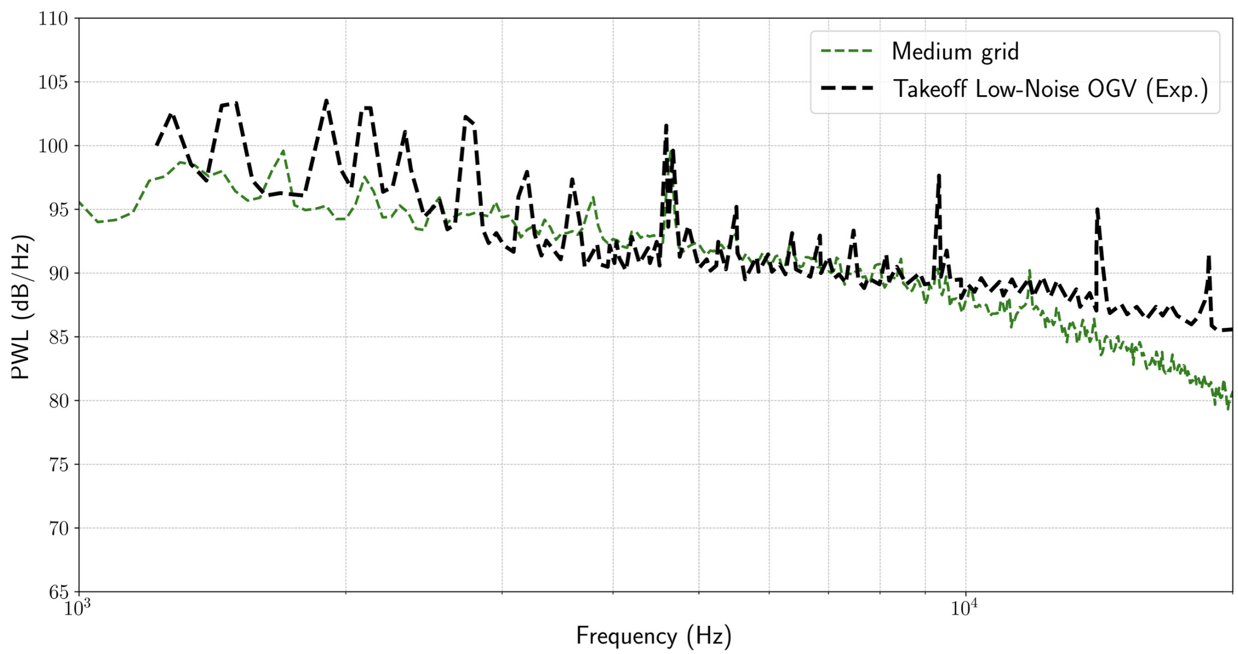

Fig. 5 PWL computed for the low-noise OGV configuration at takeoff conditions.

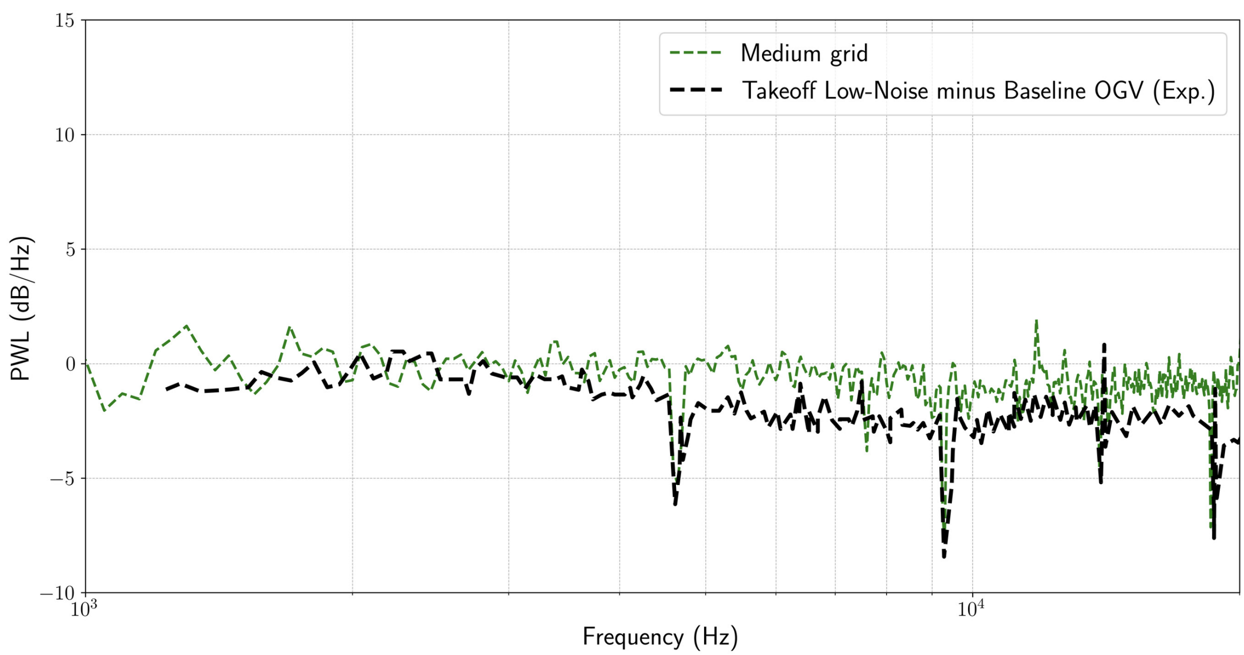

Fig. 6 Difference in PWL between the baseline OGV configuration and the low-noise OGV configuration at takeoff conditions.

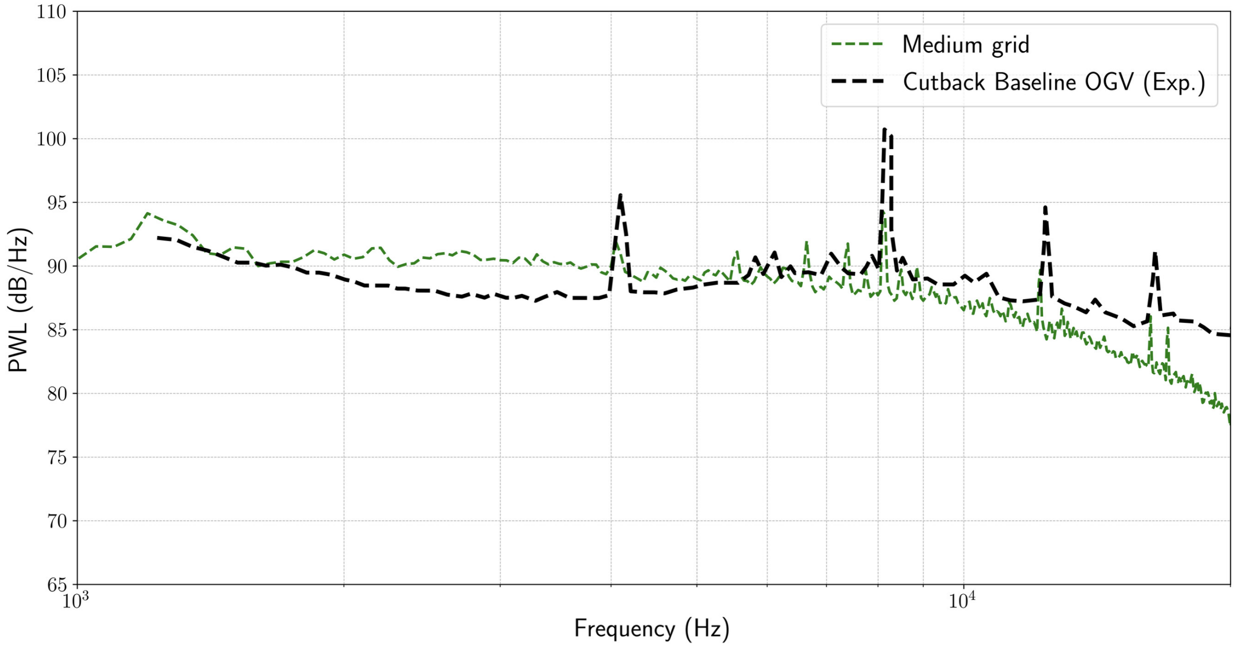

Fig. 7 PWL computed for the baseline OGV configuration at cutback conditions.

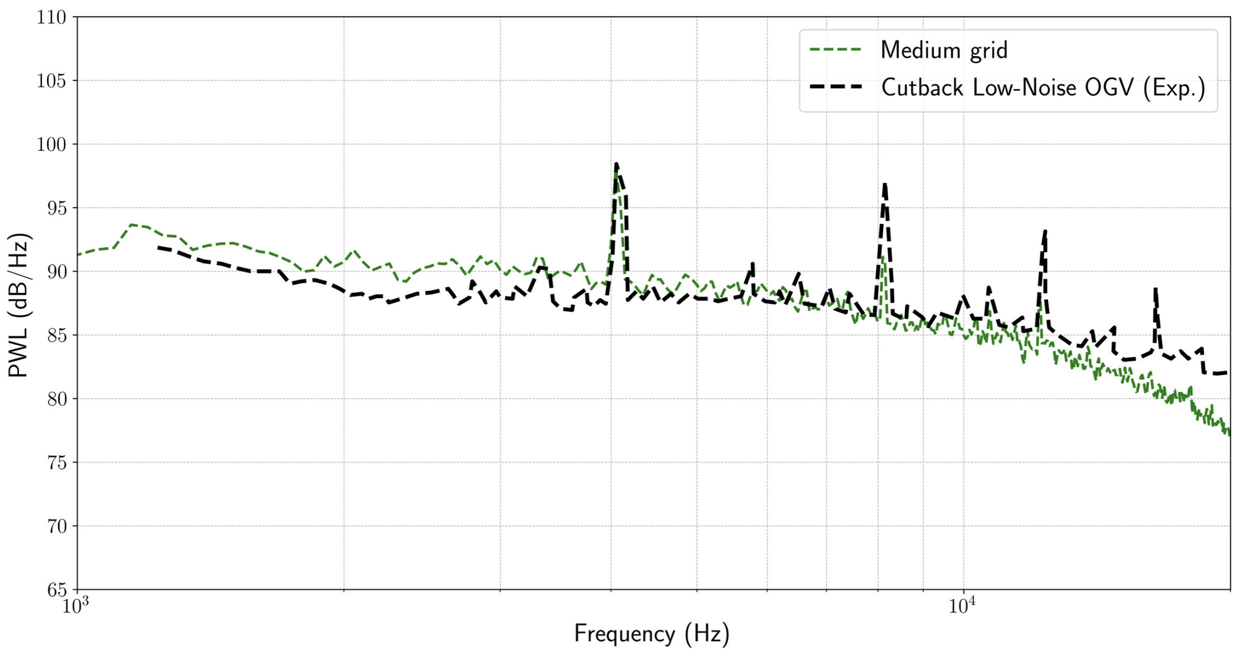

Fig. 8 PWL computed for the low-noise OGV configuration at cutback conditions.

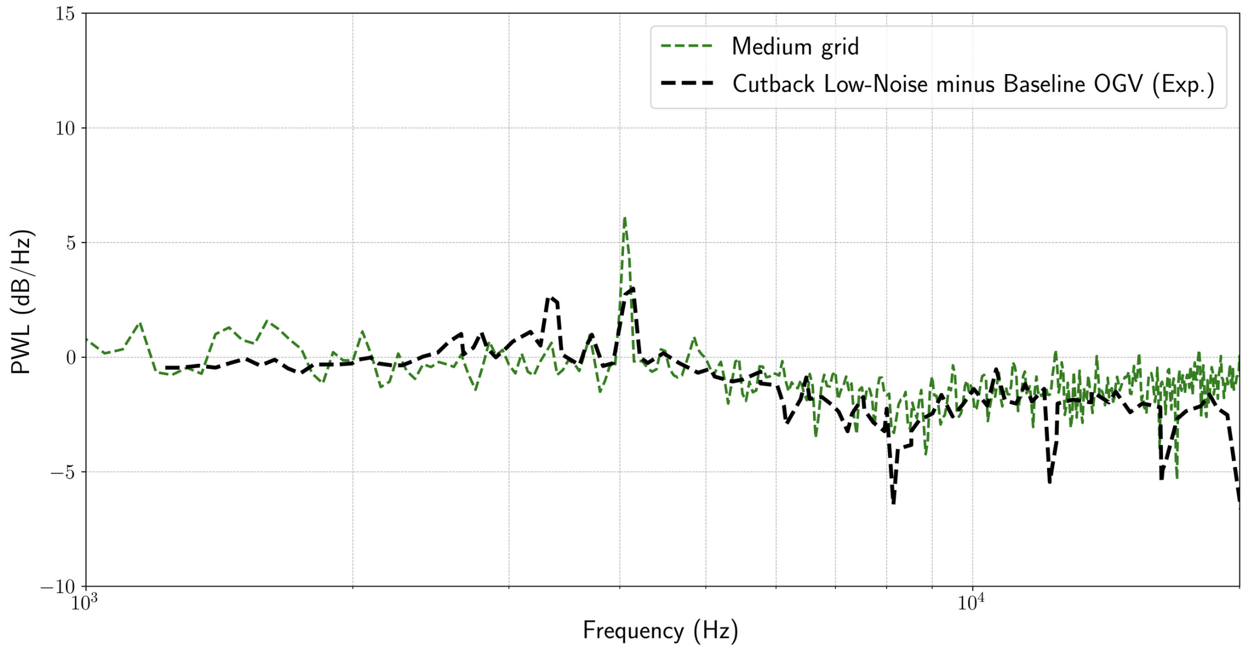

Fig. 9 Difference in PWL between the baseline OGV configuration and the low-noise OGV configuration at cutback conditions.

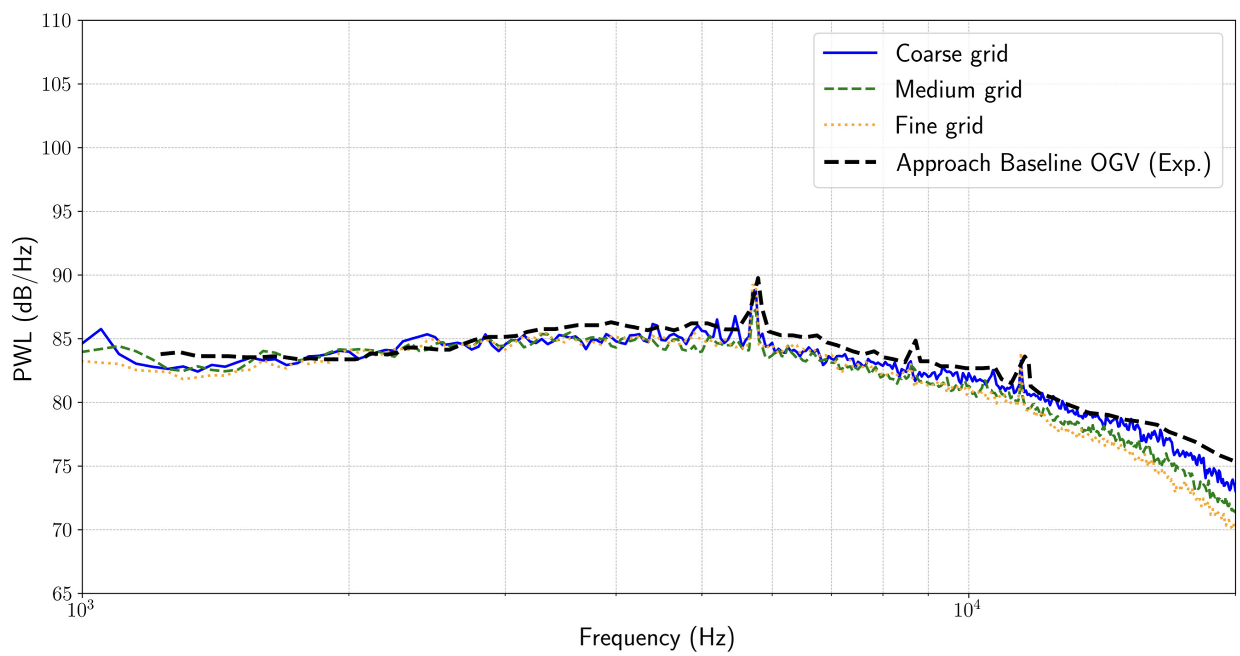

Fig. 10 PWL computed for the baseline OGV configuration at approach conditions.

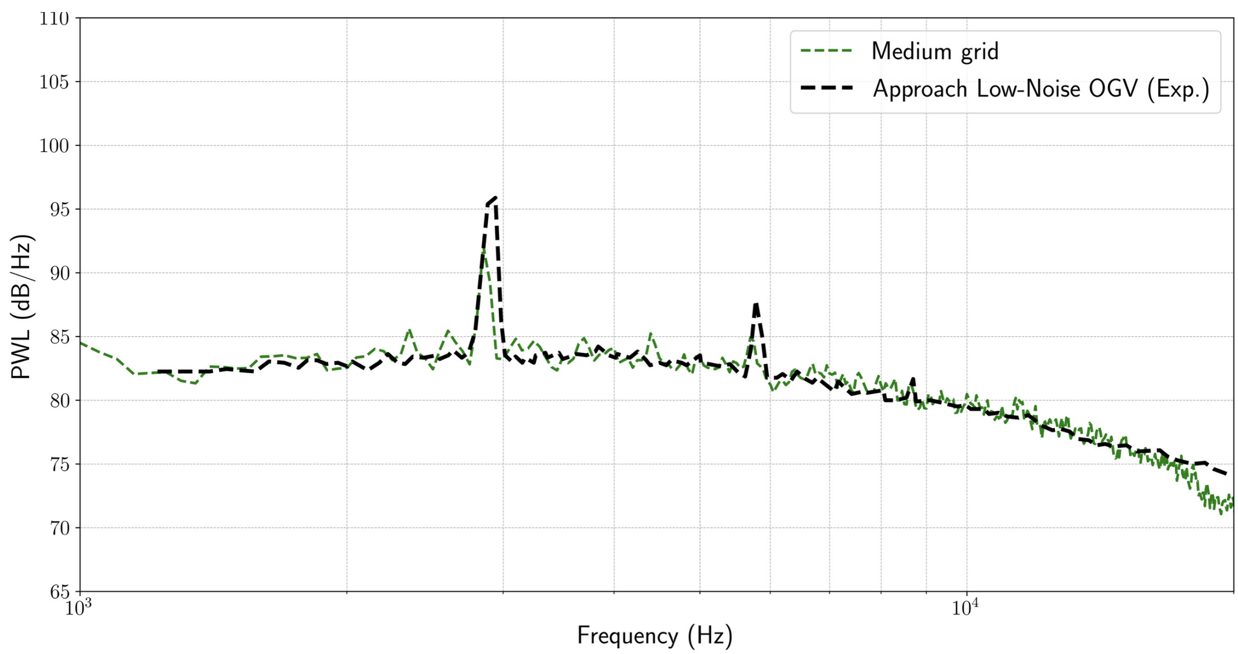

Fig. 11 PWL computed for the low-noise OGV configuration at approach conditions.

Takeoff condition (100% Design Speed)

	Mass Flow Rate	Tt Ratio	Pt Ratio
Experiment	43.998 kg/s	1.137	1.49
Coarse Grid (442M)	44.258 (+0.59%)	1.128 (-0.79%)	1.4810 (-0.7%)
Medium Grid (715M)	44.332 (+0.75%)	1.131 (-0.52%)	1.4897 (<0.1%)
Fine Grid (979M)	44.341 (+0.77%)	1.133 (-0.35%)	1.4896 (<0.1%)

Cutback condition (87.5% Design Speed)

	Mass Flow Rate	Tt Ratio	Pt Ratio
Experiment	38.011 kg/s	1.101	1.347
Medium Grid (715M)	38.052 (+0.1%)	1.0987 (-0.2%)	1.349 (+0.15%)

Approach condition (61.7% Design Speed)

	Mass Flow Rate	Tt Ratio	Pt Ratio
Experiment	26.53 kg/s	1.049	1.154
Coarse Grid (442M)	26.48 (-0.18%)	1.048 (-0.1%)	1.152 (-0.17%)
Medium Grid (715M)	26.56 (+0.1%)	1.049 (<0.1%)	1.159 (+0.4%)
Fine Grid (979M)	26.58 (+0.18%)	1.049 (<0.1%)	1.160 (+0.5%)

Fig. 12 Performance Characteristics of Baseline OGV simulations on all grids simulated for the three operating conditions. The relative errors are shown in parentheses using blue font.

agree within 1-2 dB/Hz up to 10 kHz and within 4-5 dB/Hz up to 20 kHz, with minimal sensitivity to grid resolution. Notably, the coarsest grid captures the low-frequency *buzz-saw* (multiple pure tone, MPT) features in agreement with the experiment, whereas the medium and fine grids do not. This behavior is attributed to numerical anisotropy, which diminishes with grid refinement; this aspect is discussed further later in this section.

2) For the low-noise OGV configuration at takeoff, the medium-resolution grid again shows good agreement with experimental data, with errors comparable to those observed for the baseline configuration. The difference in PWL between the baseline and low-noise configurations is shown in Fig. 6. The reduction in tonal noise due to the modified OGV design is well captured, although the broadband noise reduction is slightly underpredicted by approximately 2-3 dB/Hz.
3) The cutback condition is examined in Fig. 7 through 9. Good agreement is observed for both tonal and broadband components, with errors up to approximately 5 dB/Hz at 20 kHz. The difference between the baseline and low-noise configurations is captured accurately (Fig. 9), including the increase in the first BPF tone and the reduction in broadband noise as well as higher-order BPF harmonics.
4) The approach condition is shown in Fig. 10 and 11. Excellent agreement is observed for both configurations at this low-RPM condition, with both tonal and broadband components predicted within 2-3 dB/Hz up to 20 kHz.
5) Aerodynamic performance metrics such as the mass-flow rate, stagnation pressure and temperature ratios show reasonable agreement with all errors below 1% compared with the experiment. The increasing mass-flow rate error with grid refinement is slightly concerning - this is possibly a consequence of lack of discrete conservation obtained at viscous wall within the immersed boundary formulation used in ScaLES. More recent and upcoming improvements in ScaLES that address this deficiency are expected to address this. Nonetheless, this level of overall agreement is quite encouraging and comparable with accuracy seen in prior scale resolving simulations of this geometry [5–7].

IV. Sensitivity to Ffowcs Williams and Hawkings integration surface

While the sensitivity to FWH surface placement and the use of endcaps to account for missing quadrupole contributions (arising from flow structures exiting the FWH integration surface) has been extensively studied in jet aeroacoustics [34–36], with well-established best practices [22, 37], it has received comparatively less attention in fan noise applications. Fig. 13 illustrates the two FWH integration surfaces considered to quantify the impact of endcap averaging on the propagated acoustics. The corresponding power level spectra are shown in Fig. 14 for both the approach condition and the significantly higher-amplitude takeoff condition. As expected, the sensitivity to endcap treatment is most pronounced at low frequencies (up to approximately 2 kHz), where the averaging procedure mitigates spurious low-frequency overpredictions.

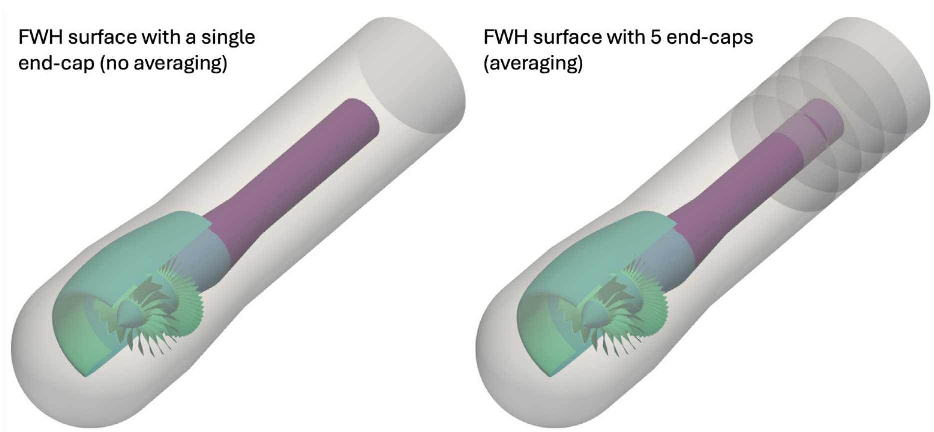

Fig. 13 Two FWH surfaces – with and without endcap averaging.

A notable feature of the Woodward et al. (2002) [11] experiments was the attempt to isolate the jet exhaust contribution from the fan inlet contribution to the overall acoustic signature. This was achieved by utilizing a *barrier wall* positioned above the turbofan, which could be traversed axially to shield different noise sources. A similar decomposition is modeled in the present simulations by partitioning the FWH surface into inlet and exhaust components

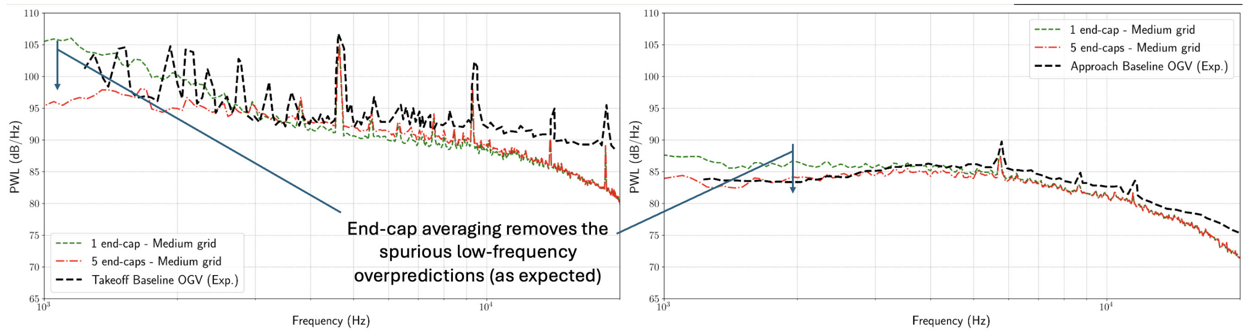

Fig. 14 Sensitivity to endcap averaging seen for PWL at two different operating conditions for the baseline OGV configuration.

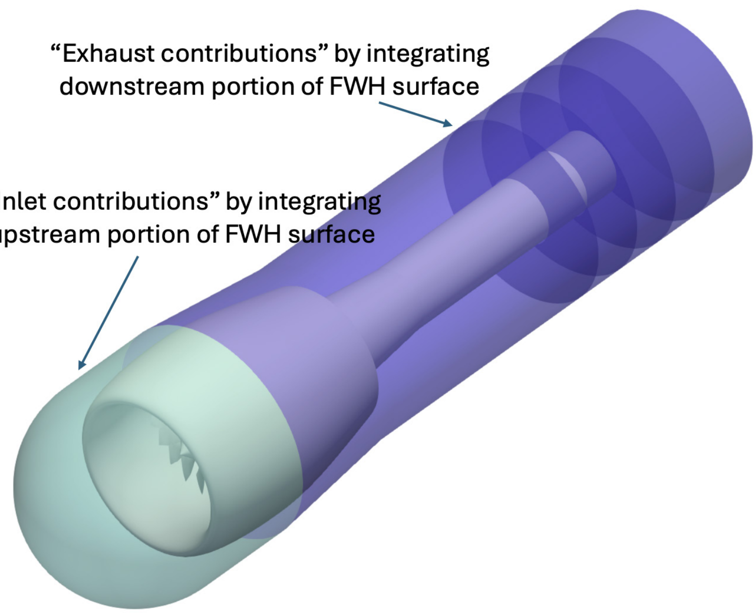

Fig. 15 Partitioning of the FWH surface into inlet and exhaust integration surfaces.

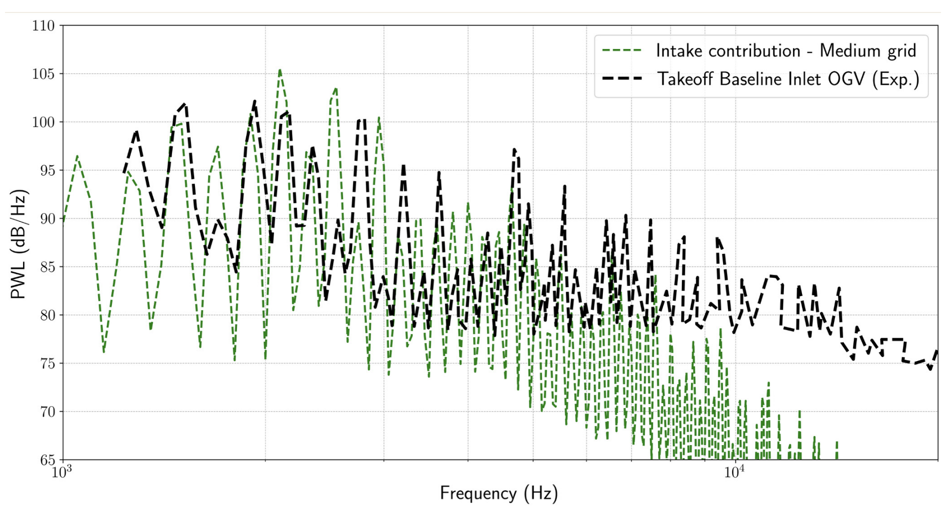

Fig. 16 Inlet contributions to total PWL compared with experiment for the takeoff conditions using the baseline OGV configuration.

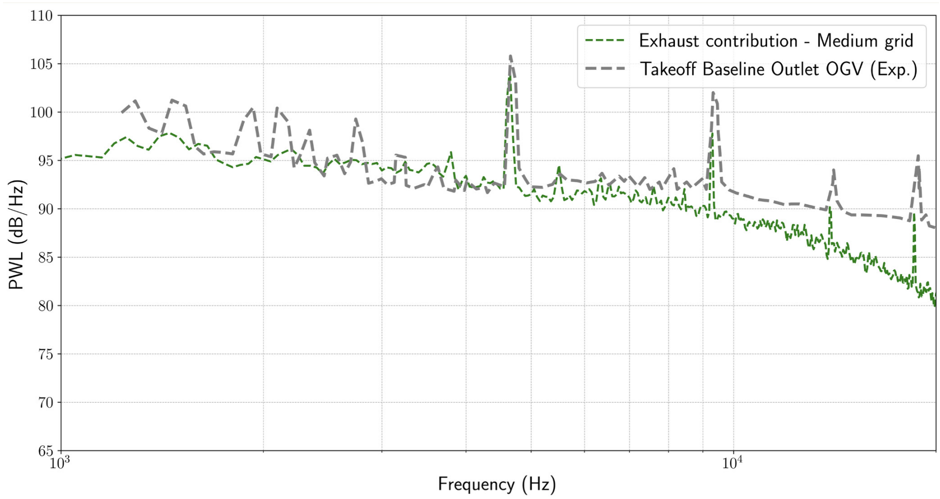

Fig. 17 Exhaust contributions to total PWL compared with experiment for the takeoff conditions using the baseline OGV configuration.

(see Fig. 15) and performing separate acoustic integrations for each surface. The resulting PWL comparisons with experimental data, shown in Fig. 16 and 17, demonstrate reasonable agreement, with discrepancies likely attributable to differences in the source-separation methodology.

Notably, the low-frequency *buzz-saw* (multiple pure tone) features are observed exclusively in the inlet contribution, whereas the BPF harmonics are predominantly associated with the exhaust contribution.

V. Multiple pure tones at supersonic tip-Mach numbers

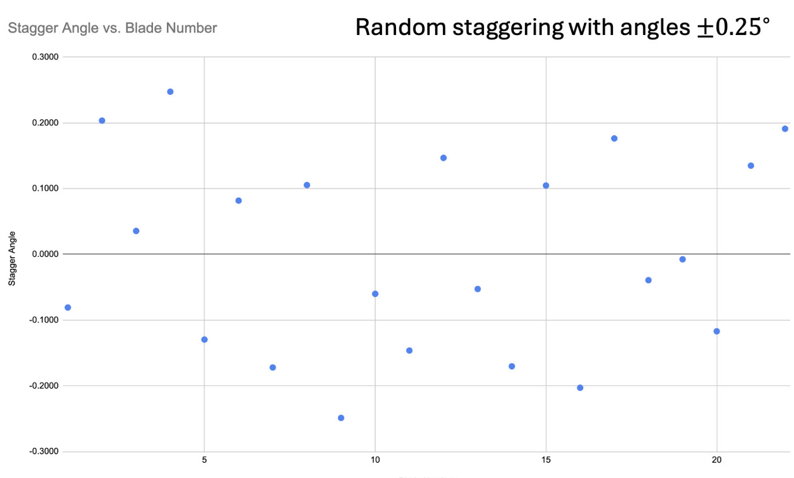

Blade Number	Azimuth Angle (deg.)	Stagger Angle (deg.)
1	0.0000	-0.0809
2	16.3636	0.2034
3	32.7273	0.0356
4	49.0909	0.2474
5	65.4545	-0.1296
6	81.8182	0.0817
7	98.1818	-0.1720
8	114.5455	0.1054
9	130.9091	-0.2488
10	147.2727	-0.0601
11	163.6364	-0.1463
12	180.0000	0.1467
13	196.3636	-0.0527
14	212.7273	-0.1703
15	229.0909	0.1047
16	245.4545	-0.2029
17	261.8182	0.1763
18	278.1818	-0.0393
19	294.5455	-0.0075
20	310.9091	-0.1170
21	327.2727	0.1349
22	343.6364	0.1910

Fig. 18 Artificial staggering added to the blades to emulate manufacturing anomalies.

To investigate the low-frequency *buzz-saw* modes, artificial blade staggering is introduced, with each of the 22 blades assigned a random angular offset of up to ±0.25°. This approach follows Gonzalez-Martino et al. (2018) [6] and is intended to emulate manufacturing variability in turbofan blades. Such small perturbations do not produce statistically significant changes in aerodynamic performance but are expected to influence noise generation at supersonic tip Mach numbers through non-periodic and partially decorrelated shock interactions.

Fig. 20 and 21 demonstrate the emergence of low-frequency buzz-saw tones due to these perturbations, in agreement with experimental observations. This also provides insight into the buzz-saw modes observed on the coarse grid. The

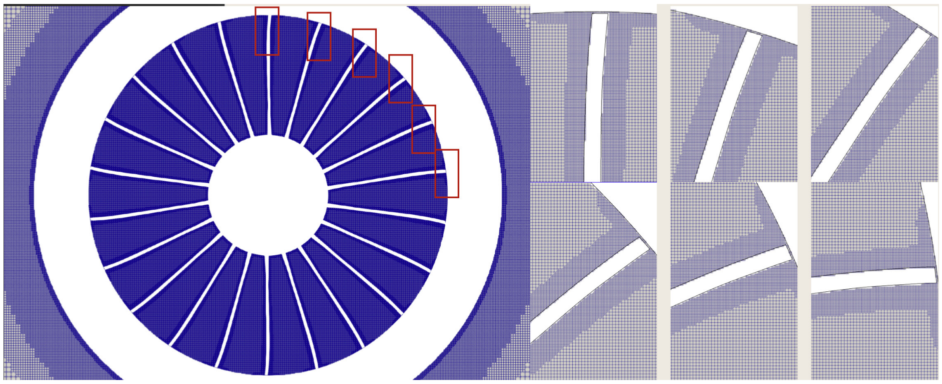

Fig. 19 Numerical staggering of the blades caused by the immersed boundary method and non-body aligned grids. Even though all 22 blades are identical, there are 6 distinct numerical blade topologies that are observed.

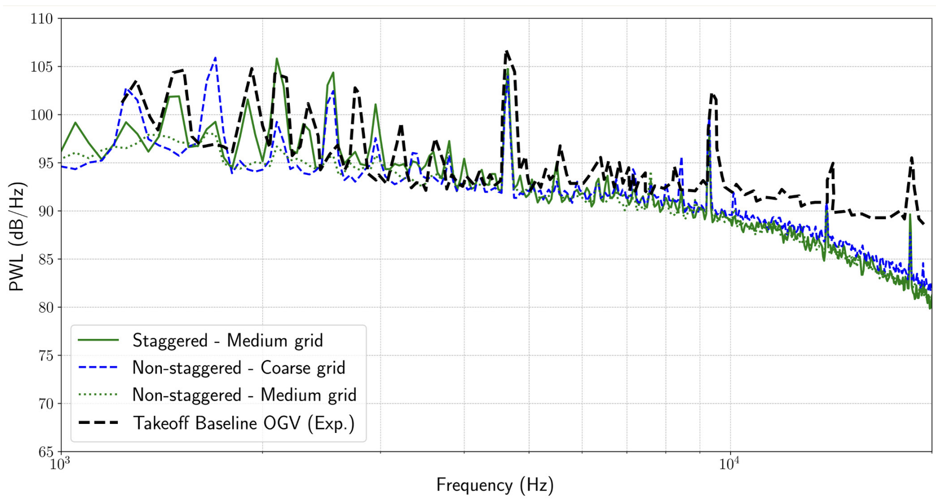

Fig. 20 PWL comparing the effect of artificial blade staggering triggering low-frequency buzz-saw modes (multiple pure tones).

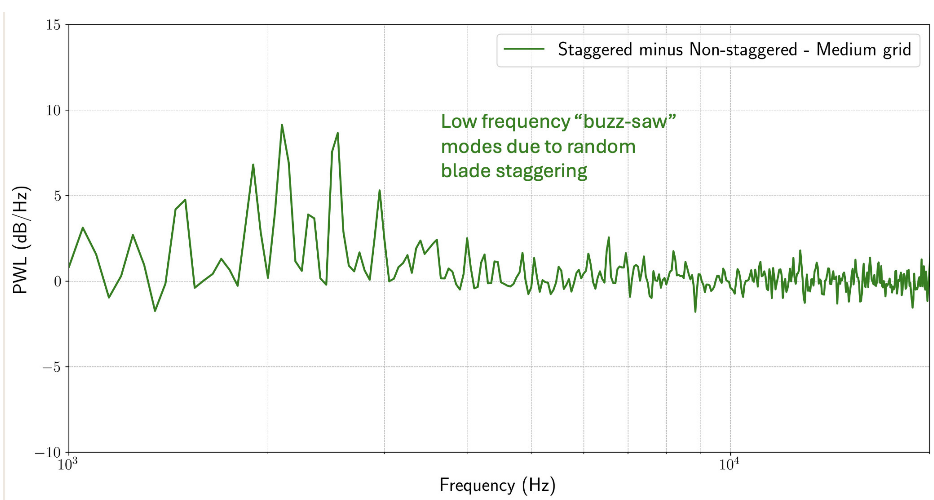

Fig. 21 PWL difference between the staggered and non-staggered conditions on the medium grid at takeoff conditions showing the additional low-frequency energy observed in the buzz-saw modes.

use of an immersed boundary representation within a Cartesian octree framework results in a non-body-conformal discretization of the blade geometry (Fig. 19). For the 22-blade rotor, this leads to six distinct numerical blade topologies even when the underlying geometry is identical.

Although these topological differences persist at all resolutions, the associated discretization errors decrease with grid refinement, consistent with second-order convergence. As a result, the numerical representations of the blades become increasingly similar, and the spurious multiple pure tone (MPT) content diminishes. This explains why, in the absence of geometric perturbations, the artificially induced MPT observed on coarse grids decreases with refinement. In contrast, physically motivated blade staggering is required to recover buzz-saw tones consistently across grid resolutions.

VI. Role of off-body volume grid resolution

One of the consistent trends observed in the PWL comparisons with experimental data in the previous section is the systematic underprediction of high-frequency noise (> 10 kHz). This discrepancy is particularly pronounced at high RPM conditions and does not appear to be sensitive to the near-wall surface refinement discussed in Section III. Consequently, the present section seeks to isolate the source of this high-frequency deficit and assess targeted grid refinement strategies to address it.

Since the metric of interest—the propagated noise power (PWL)—is obtained via FWH integration, any modifications to the volume grid must be considered in conjunction with the improvements to the FWH surface.

A. Aft grid resolution: vortical flow from rotor wake and the nacelle shear-layer

As an initial step, volume grid refinement is focused on the region downstream of the rotor and OGV, which are expected to be dominant contributors to broadband noise. Four grid configurations are considered, along with two FWH surfaces:

1) Grid B (715M cells): Baseline (“medium”) grid discussed in Section III.
2) Grid B+ (947M cells): Enhanced refinement downstream of the rotor stacking axis (see highlighted region in Fig. 22).
3) Grid B++ (924M cells): Reduced downstream refinement compared to B+, with additional localized refinement at the nacelle tip, where the shear layer is a known source of high-frequency broadband noise.
4) Grid B’ (985M cells): A contrasting strategy in which the finest near-wall resolution at the rotor is removed and a global refinement by a factor of 1.33 is applied. This results in coarser wall resolution but finer resolution throughout the off-body volume.

Although these grids have comparable total cell counts, they differ significantly in topology and resolution distribution (Fig. 22). In addition to the baseline FWH surface, a “tighter” FWH surface is introduced, featuring approximately twice the spatial sampling resolution. This surface is designed to better capture acoustic sources in refined regions of the volume grid while avoiding spatial aliasing. The endcaps are also extended further downstream to minimize artificial filtering (Fig. 23).

Fig. 24 presents PWL comparisons for the baseline OGV configuration at takeoff conditions across combinations of grid topologies and FWH surfaces. Surprisingly, minimal sensitivity is observed between Grids B, B+, and B++ for either FWH surface. In contrast, Grid B’ shows a modest reduction in the high-frequency drop-off despite degraded aerodynamic accuracy due to coarser near-wall resolution. This indicates that improvements in high-frequency acoustic prediction are not strongly linked to aft-region refinement or FWH surface placement, but instead to global off-body resolution.

To further investigate this behavior, power spectral density (PSD) comparisons are examined directly at microphone locations, rather than relying solely on the integrated PWL metric. For clarity, the analysis is restricted to two representative setups:

- Setup A: Grid B with baseline FWH surface (reference configuration from Sections III-V).
- Setup B: Grid B++ with tighter FWH surface (enhanced aft-resolution configuration).

Fig. 25 shows the microphone arrangement used in the 9- by 15-Ft Low Speed Wind Tunnel (LSWT) [38] at NASA Glenn Research Center. Fig. 26 through 28 compare PSD spectra at three representative microphone locations. These comparisons reveal several key insights:

1) Downstream microphones exhibit excellent agreement for both operating conditions and both setups, with accurate prediction of tonal and broadband content up to frequencies exceeding 20 kHz. This indicates that downstream-propagating noise is well captured and is not responsible for the high-frequency deficit observed in PWL.

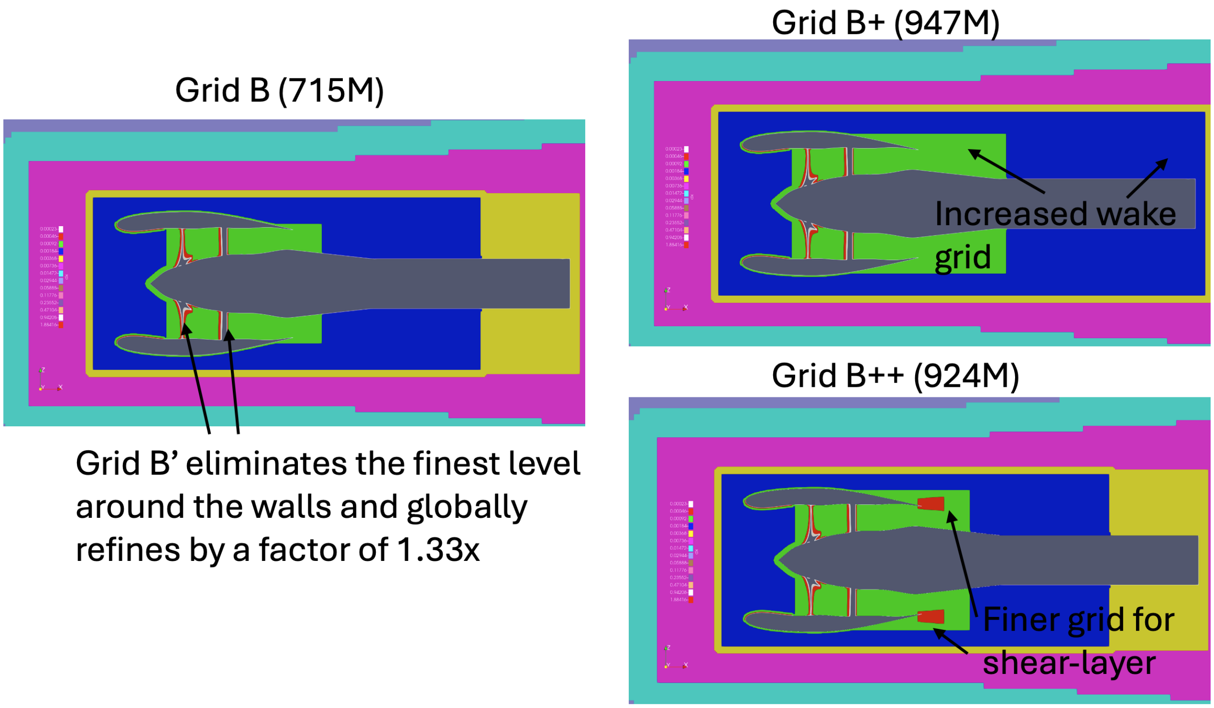

Fig. 22 Four grid topologies comparison – the baseline grid B with three further modifications.

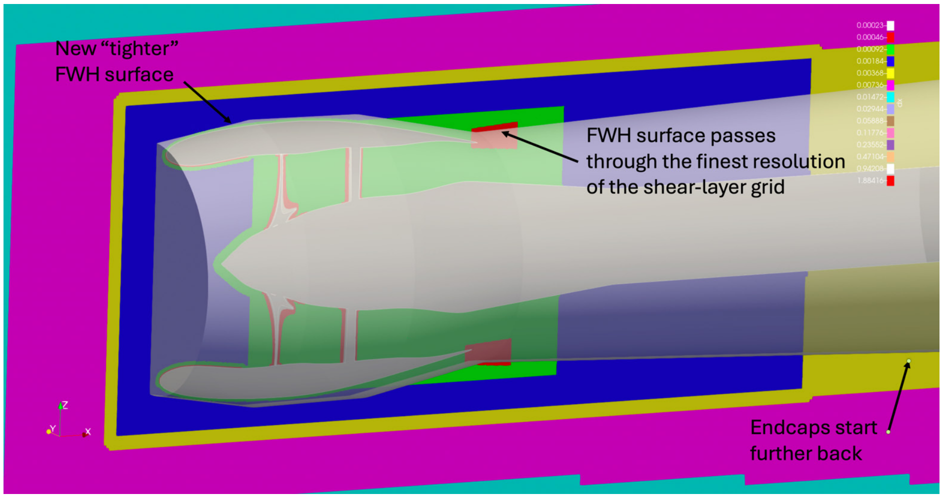

Fig. 23 The new *tighter* FWH surface used with enhanced spatial sampling and extended downstream endcaps.

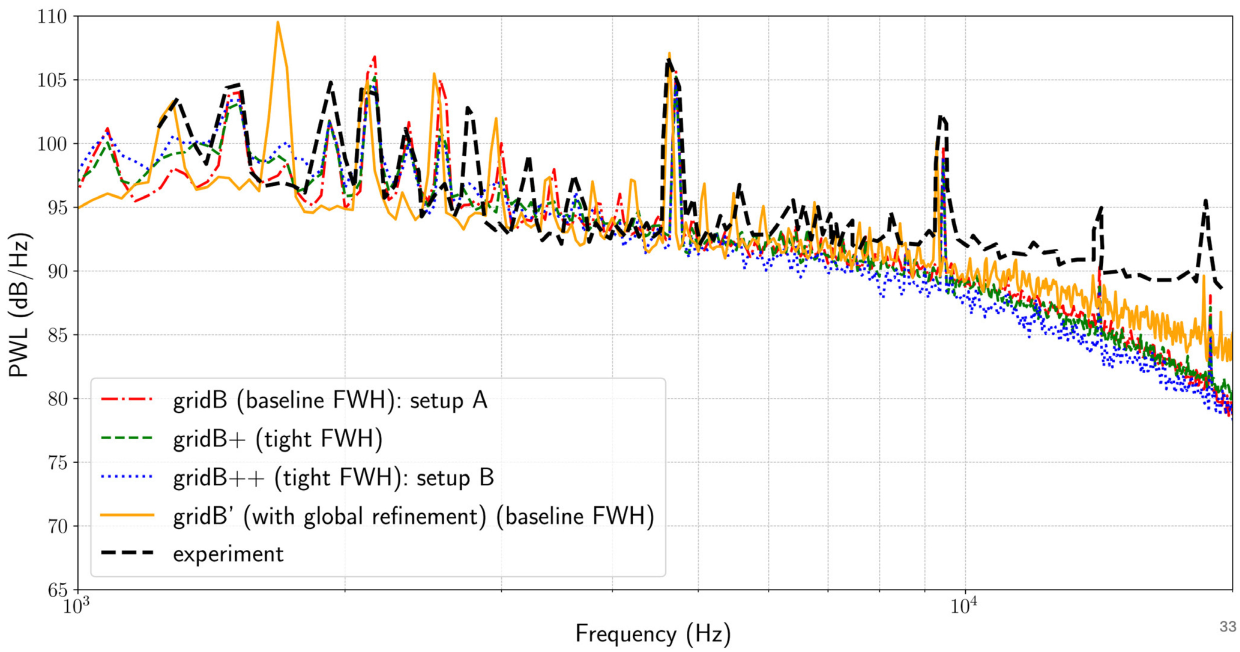

Fig. 24 Sound power level (PWL) obtained for the baseline OGV configuration at takeoff conditions on various combinations of FWH surfaces and volume grid topologies.

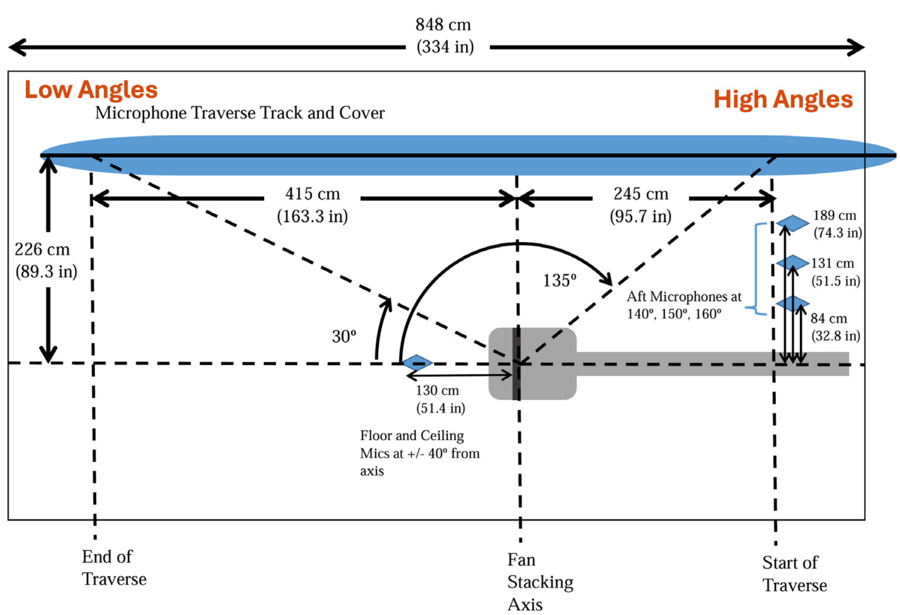

Fig. 25 Microphone setup on the linear array relative to the model geometry position. Figure taken from Brown & Stephens (2018) [38].

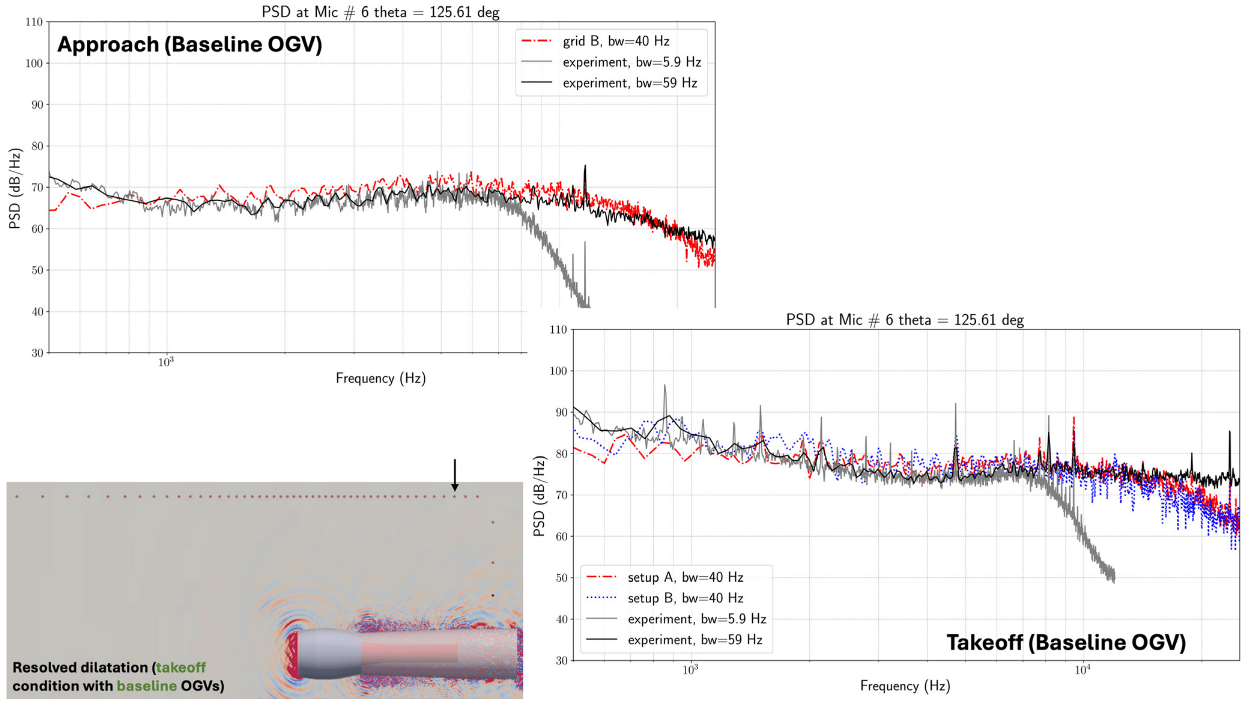

Fig. 26 PSD comparisons at Microphone 6 located at θ = 125.61° for the baseline OGV configuration.

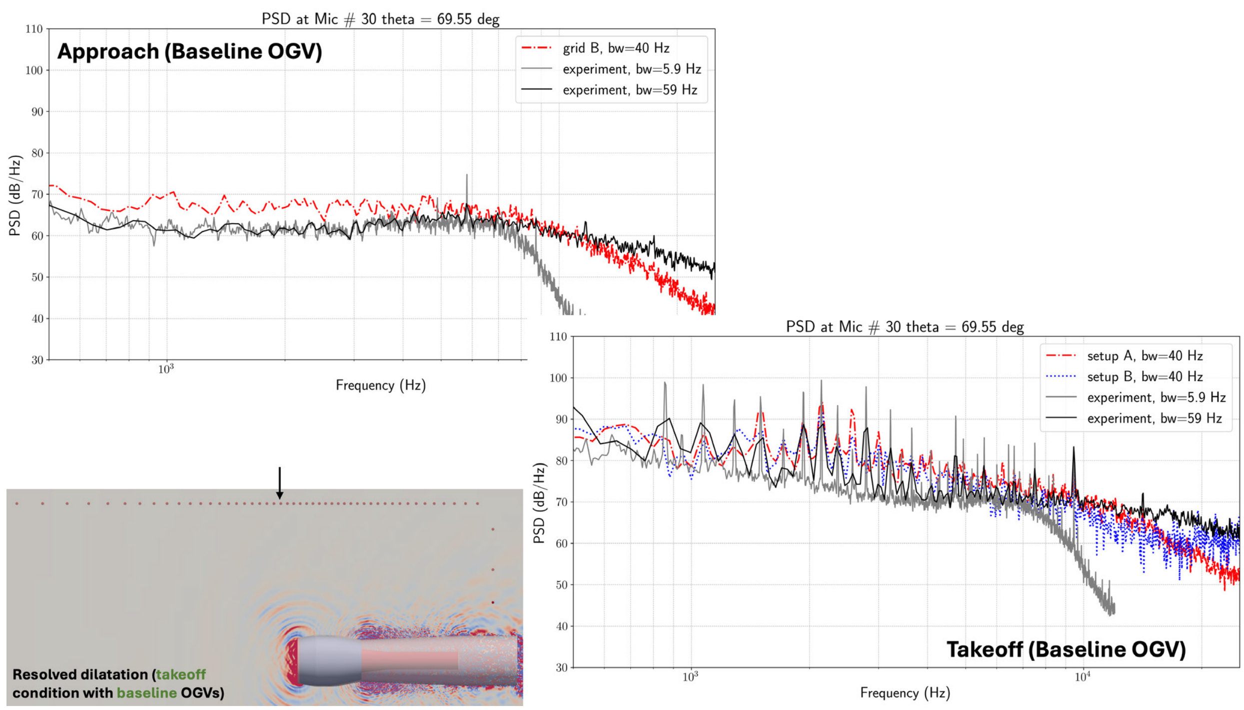

Fig. 27 PSD comparisons at Microphone 30 located at θ = 69.55° for the baseline OGV configuration.

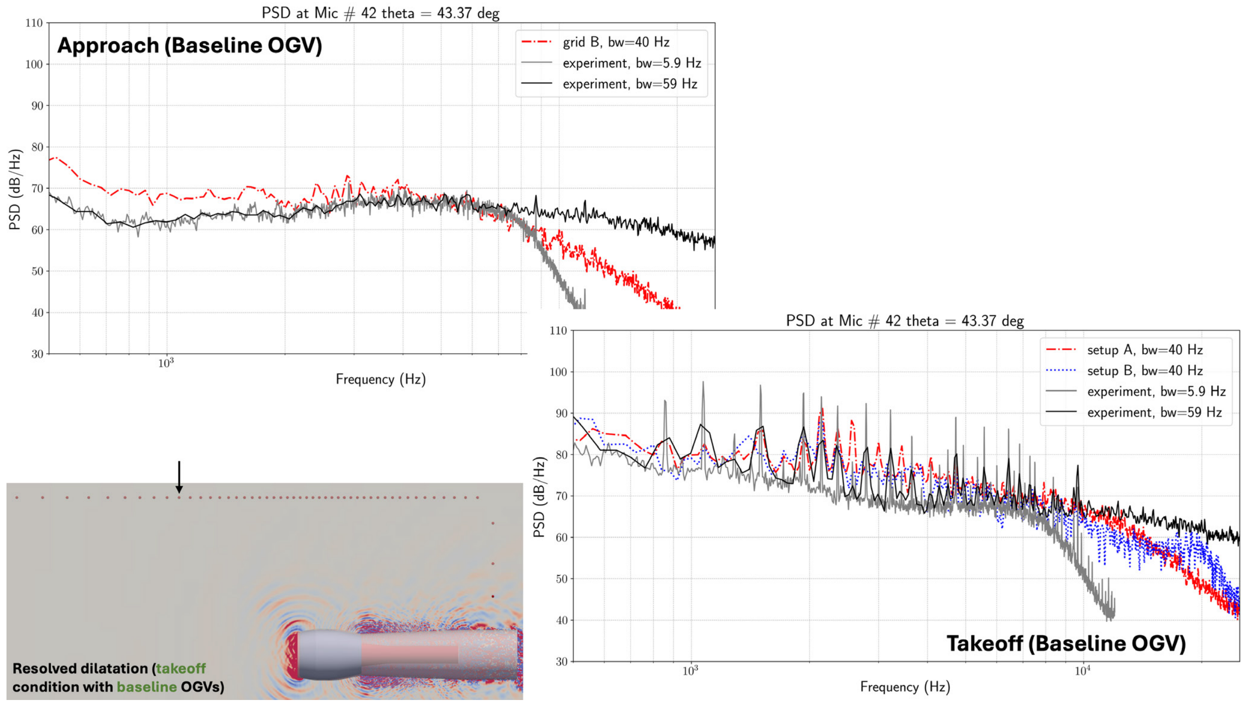

Fig. 28 PSD comparisons at Microphone 42 located at θ = 43.37° for the baseline OGV configuration.

2) The microphone located near the nacelle entrance (θ = 70°) shows moderate high-frequency underprediction, more pronounced for the approach condition than for takeoff.
3) The upstream-most microphone (θ = 42°) exhibits a clear and consistent underprediction of high-frequency content, particularly for the approach condition. In contrast, the low-frequency buzz-saw tones are well captured at these locations.
4) Although the upstream high-frequency deficit is significant for the approach condition, its impact on the integrated PWL is muted because the overall acoustic energy is dominated by downstream contributions, which are accurately predicted. This is not the case for the takeoff condition where the upstream traveling non-linear waves contribute a significant portion of the total radiated acoustic energy.

These results suggest that the baseline grid provides sufficient resolution to capture aerodynamic performance and downstream-propagated noise, including vortical structures in the wake region. However, it remains insufficient for accurately resolving upstream-propagating acoustic waves originating near the rotor and propagating through the duct.

B. Upstream grid resolution: irrotational flow in the duct

Building on the observations from the previous section, the first refinement strategy considered is uniform grid refinement in the upstream duct region. For this study, the tighter FWH surface is employed, and Grid B+ is adopted as the baseline (hereafter referred to as the "old mesh"). The comparison between the old and refined ("new") grid is shown in Fig. 29.

This upstream refinement introduces a substantial increase in grid cells, although the minimum grid spacing—and therefore the time-step size—remains unchanged. Fig. 30 through 32 show the resulting improvements in PSD at the upstream microphones. In particular, a significant improvement is observed for the approach condition at Microphones 30 and 42. As expected, the downstream microphone predictions (e.g., Microphone 6 in Fig. 30) remain largely unaffected.

While this refinement successfully improves upstream-propagated acoustics, it incurs a significant computational cost, with the new grid containing approximately 88% more cells than the baseline. This motivates the question of whether the grid can be optimized in conjunction with the FWH surface to reduce cost while retaining accuracy.

The key idea is to reposition the FWH surface closer to the dominant noise sources (the rotor) while ensuring it remains outside regions of significant quadrupole activity. By doing so, the extent of the upstream refined region

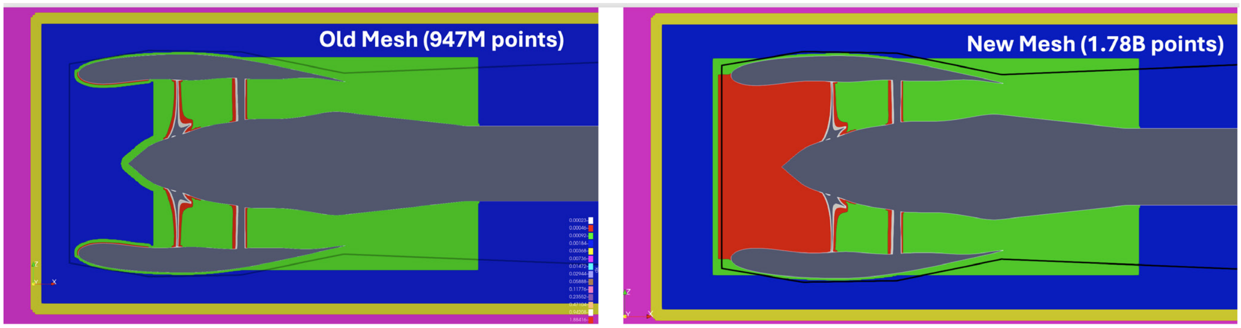

Fig. 29   Improved "new mesh" which adds more volume grid refinement upstream of the rotor.

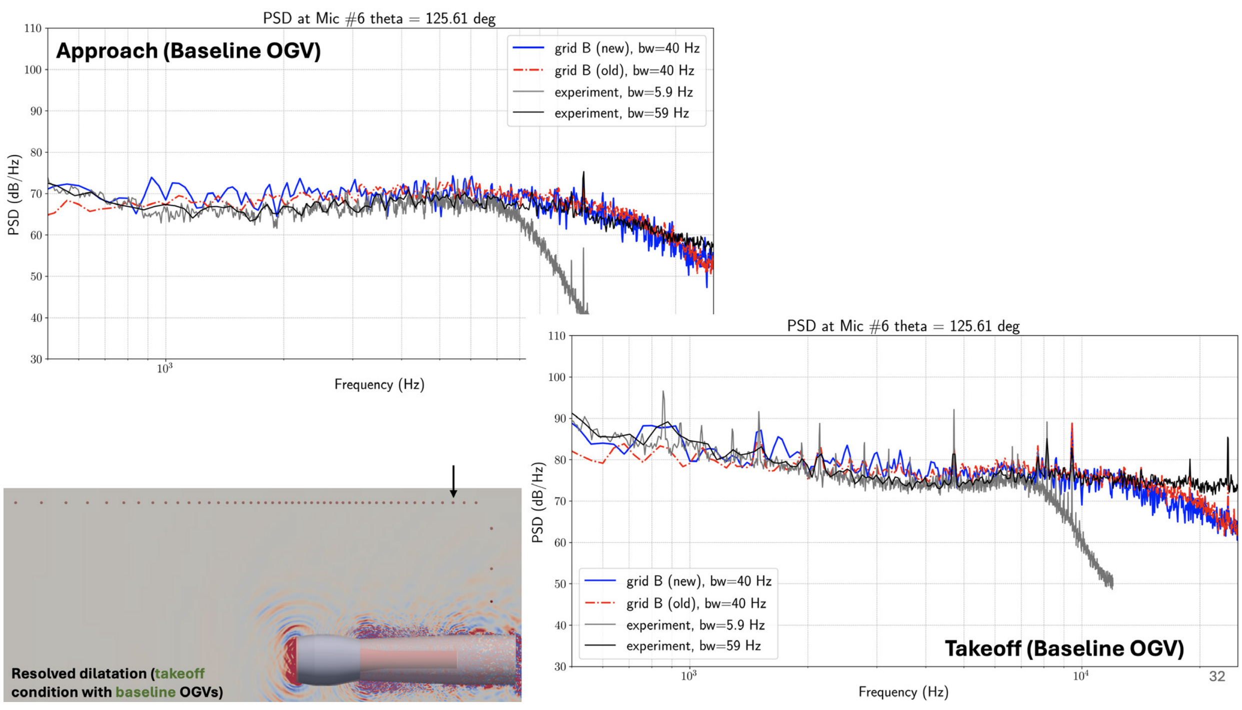

Fig. 30   PSD comparisons between old and the improved (new) grid at Microphone 6 located at θ = 125.61° for the baseline OGV configuration.

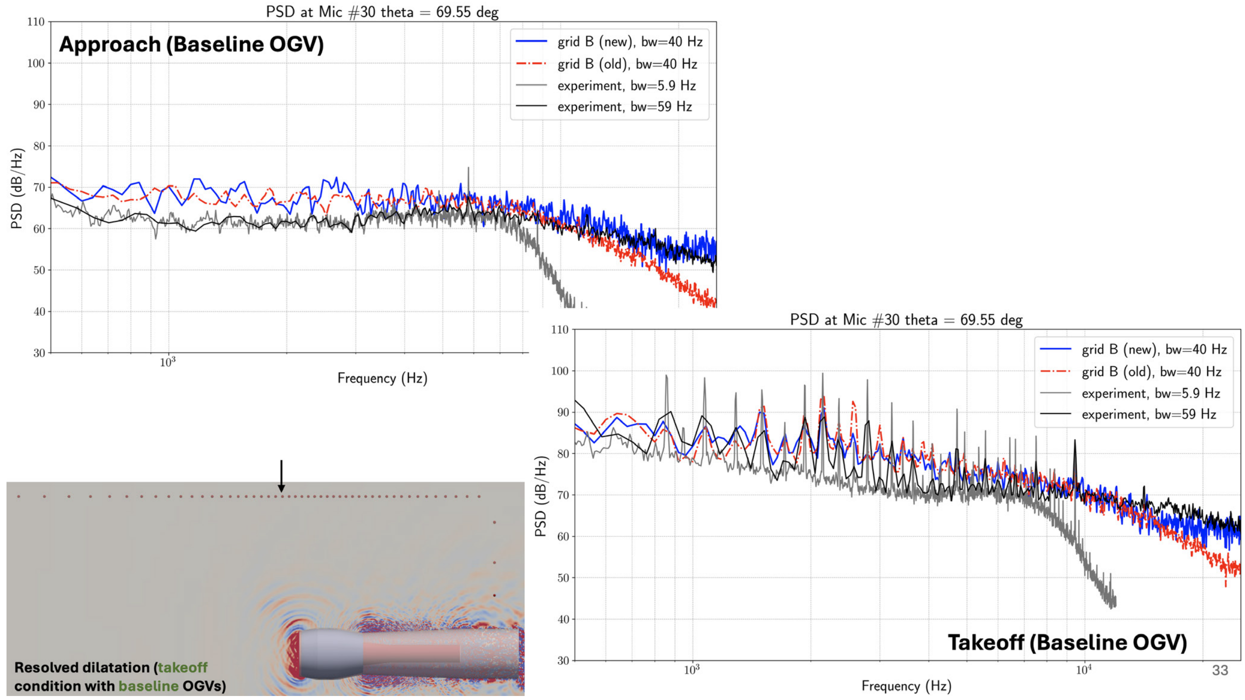

Fig. 31 PSD comparisons between old and the improved (new) grid at Microphone 30 located at θ = 69.55° for the baseline OGV configuration.

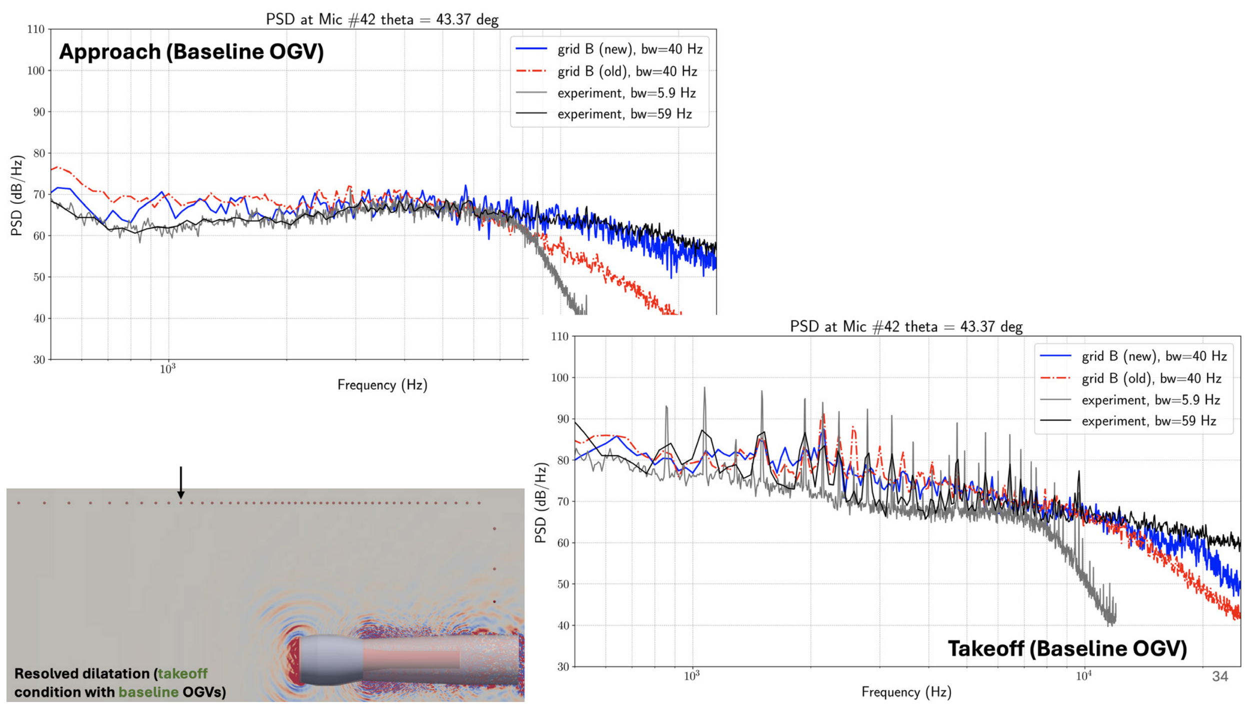

Fig. 32 PSD comparisons between old and the improved (new) grid at Microphone 42 located at θ = 43.37° for the baseline OGV configuration.

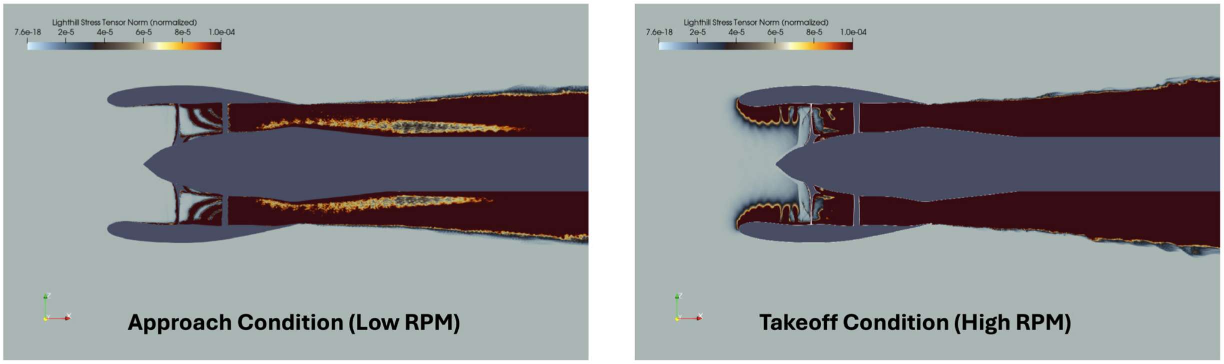

Fig. 33 Frobenius norm of the inviscid and grid-resolved contributions to the Lighthill stress tensor.

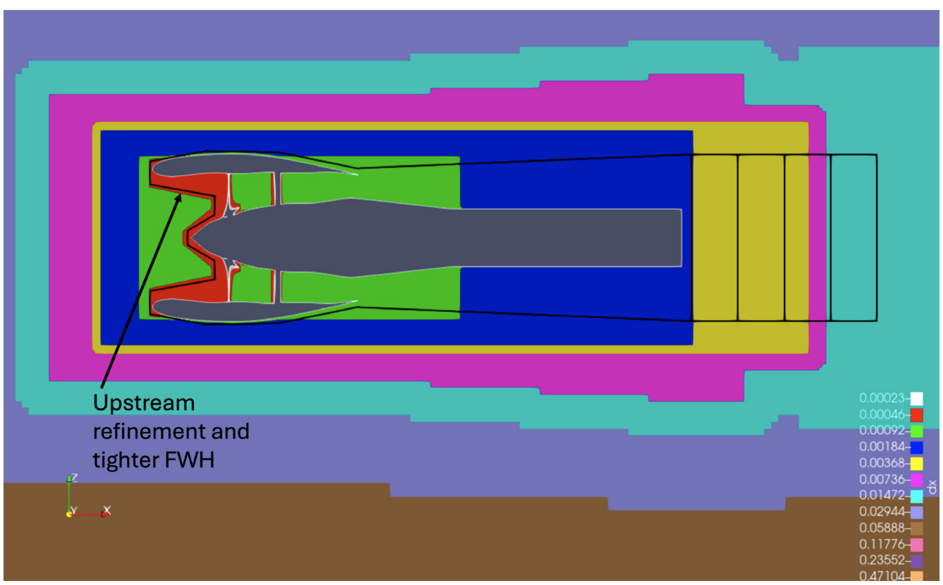

Fig. 34 Grid adapted to accommodate the use of a tighter FWH surface consistent with the spatial support of quadrupole sources.

(highlighted in Fig. 29) can be reduced. As a proof of concept, this strategy is implemented with the FWH surface placement guided by the spatial support of the Lighthill stress tensor, visualized via its Frobenius norm.

Fig. 33 shows the distribution of quadrupole source regions for both takeoff and approach conditions. Notably, these regions extend upstream due to nonlinear (shock-related) and non-barotropic effects (e.g., cowl/nacelle boundary layers), as well as contributions from resolved Reynolds stresses. Based on this information, an optimized grid and corresponding FWH surface are constructed (Fig. 34) to closely envelop the quadrupole source region within the upstream duct.

The resulting PSD at the upstream-most microphone is shown in Fig. 35. The optimized configuration achieves high-frequency accuracy comparable to that of the fully refined grid (approximately 1.6B cells) shown in Fig. 29, but with significantly reduced computational cost.

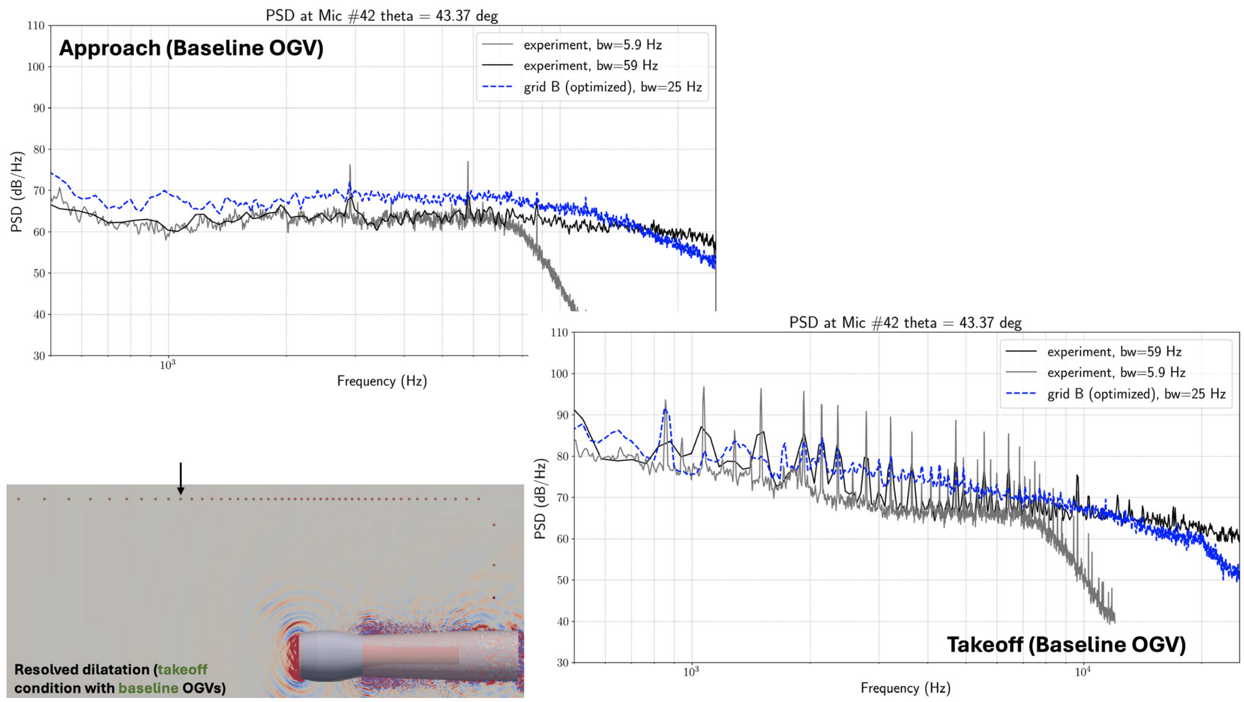

Fig. 35 PSD obtained on the optimized grid at Microphone 42 located at $\theta = 43.37°$ for the baseline OGV configuration.

VII. Summary

A systematic evaluation of Volcano ScaLES was performed for both aerodynamic performance and aeroacoustic prediction of the NASA Source Diagnostic Test. Grid refinement strategies were categorized into two classes: a) near-body refinement to accurately capture blade loading and boundary layer physics, and b) off-body refinement targeting vortical structures (wakes and shear layers) and acoustic wave propagation.

Excellent agreement with experimental data was obtained for both sound power levels and aerodynamic performance metrics (mass flow rate, stagnation pressure, and temperature). While results from the baseline grid topology were consistent with prior LES studies [6, 9], the observed underprediction of high-frequency noise (> 10 kHz) was identified and investigated. This deficiency was traced to insufficient volume resolution in the upstream duct region.

To address this, a grid optimization and FWH surface placement strategy was developed based on the spatial support of quadrupole noise sources, characterized using the Frobenius norm of the Lighthill stress tensor. The optimized configuration yields excellent agreement with experimental high-frequency noise levels across operating extremes (approach and takeoff conditions), while significantly reducing computational cost relative to uniformly refined grids.

The simulations also accurately reproduce the impact of reduced-count, swept OGV configurations on both tonal and broadband noise across all operating conditions (see Fig. 36 and 37).

Exceptional computational efficiency of the approach is demonstrated through large-scale LES on the order of

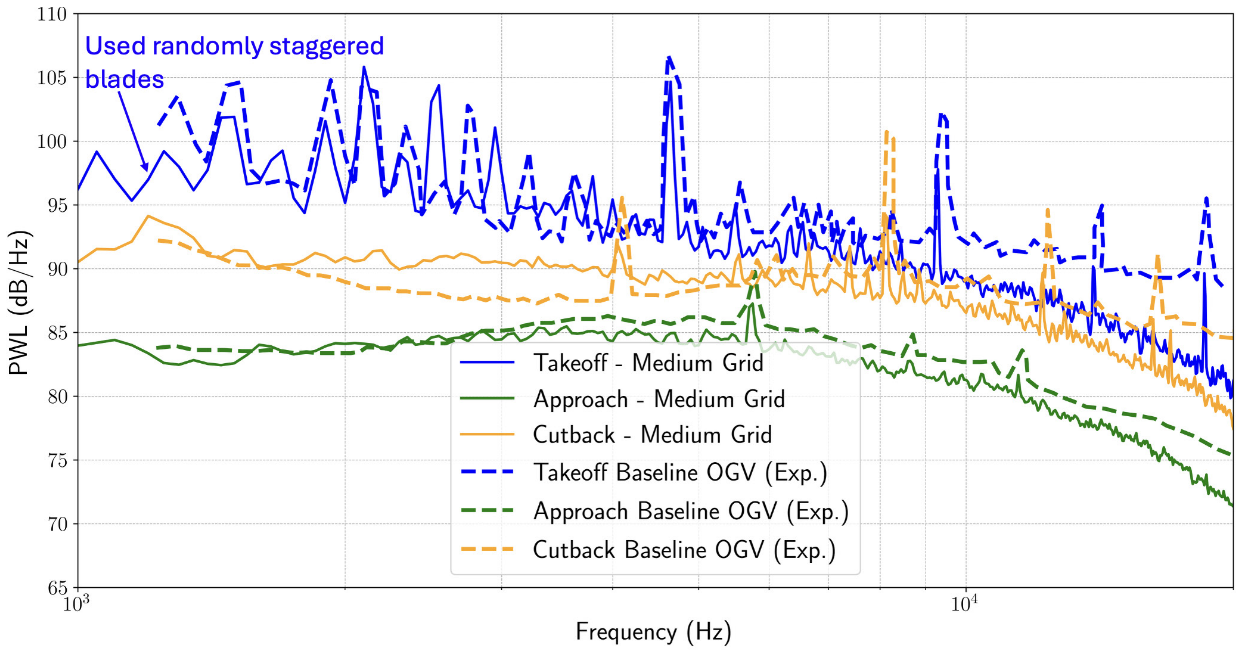

Fig. 36 PWL shown for all 3 operating conditions for the baseline OGV configuration.

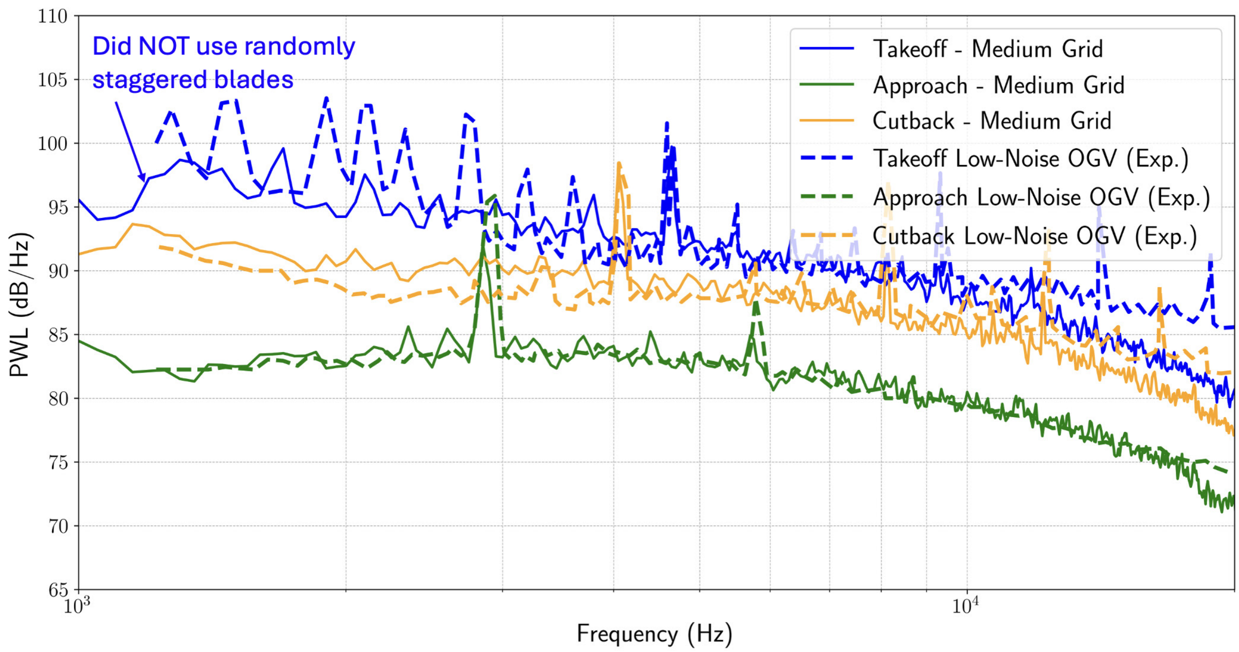

Fig. 37 PWL shown for all 3 operating conditions for the low-noise OGV configuration.

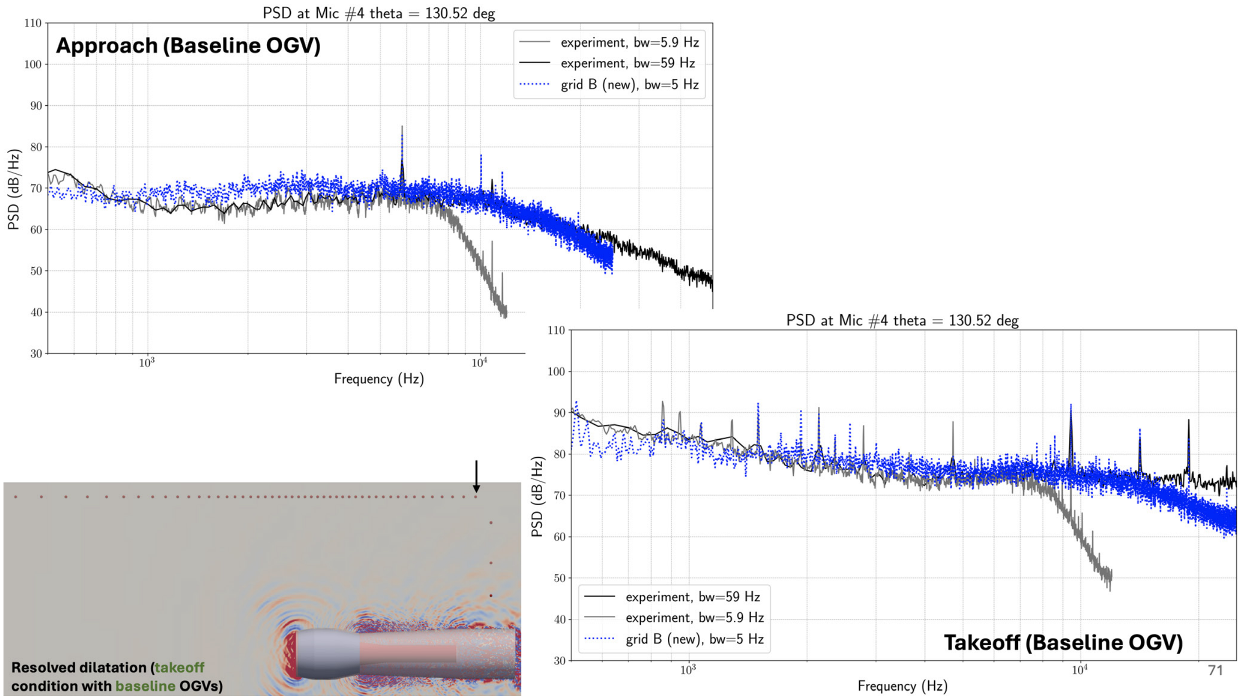

Fig. 38 PSD at Microphone 4 computed using long-time integration simulations for the Baseline OGV case.

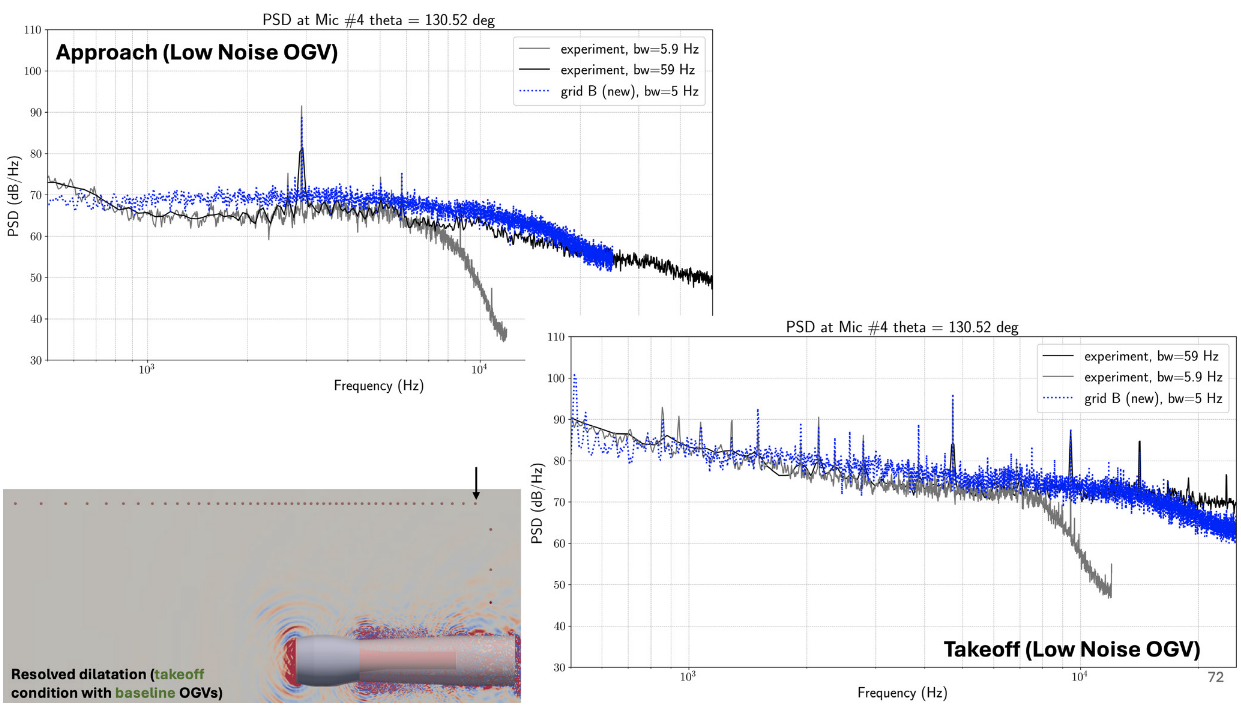

Fig. 39 PSD at Microphone 4 computed using long-time integration simulations for the low-noise OGV case.

$O(10^9)$ grid cells, performed on a single node equipped with 8 × NVIDIA L40S GPUs, with turnaround times of approximately 12-15 hours per simulation. More recent hardware (e.g., NVIDIA RTX Pro 6000 Blackwell GPUs) further reduces wall-clock time by approximately 40%. These performance characteristics significantly enhance the feasibility of LES for industrial applications.

In particular, the reduced cost per simulated rotor revolution enables long-duration simulations, facilitating convergence of low-frequency spectral content. As a demonstration, simulations exceeding 100 rotor revolutions were completed in approximately 6 days on a single node (8 × RTX Pro 6000), with resulting spectra shown in Fig. 38 and 39 computed with an unprecedented $\Delta f = 5$ Hz.

Finally, the results demonstrate that accurate fan aeroacoustic prediction with LES requires coordinated design of volume resolution and FWH surfaces, particularly for upstream-propagating high-frequency content.

VIII. Acknowledgments

This work has been supported by NASA Small Business Innovation Research (SBIR) Phase-I and Phase-II programs with contract numbers: 80NSSC24PB479 and 80NSSC25C0002 respectively. We gratefully acknowledge Dr. David Stephens of the NASA Glenn Research Center for serving as the technical monitor, sharing the experimental data, and providing insightful contributions. We also greatly appreciate Dr. Edmane Envia of NASA Glenn Research Center for his valuable discussions.

References

[1] Hughes, C. E., "NASA collaborative research on the ultra high bypass engine cycle and potential benefits for noise, performance, and emissions," *International Symposium on Air Breathing Engines (ISABE 2009)*, 2013.

[2] Hultgren, L. S., "Emerging importance of turbine noise," *International Journal of Aeroacoustics*, Vol. 10, No. 1, 2010, pp. i–iv.

[3] Nesbitt, E., "Towards a quieter low pressure turbine: design characteristics and prediction needs," *International Journal of Aeroacoustics*, Vol. 10, No. 1, 2010, pp. 1–15.

[4] Suzuki, T., Spalart, P. R., Shur, M. L., Strelets, M. K., and Travin, A. K., "Unsteady simulations of a fan/outlet-guide-vane system: broadband-noise computation," *AIAA Journal*, Vol. 57, No. 12, 2019, pp. 5168–5181.

[5] Brès, G. A., Wang, K., Ivey, C. B., Bose, S. T., Okubo, G., Kamatsuchi, T., and Tanaka, H., "Predictions of Fan Noise and Performance at Transonic Operating Conditions Using GPU-Accelerated Large-Eddy Simulations," *30th AIAA/CEAS Aeroacoustics Conference (2024)*, 2024, p. 3162.

[6] Gonzalez-Martino, I., and Casalino, D., "Fan tonal and broadband noise simulations at transonic operating conditions using lattice-Boltzmann methods," *2018 AIAA/CEAS aeroacoustics conference*, 2018, p. 3919.

[7] Fernandes, L. S., Housman, J. A., Kenway, G. K., Stich, G.-D., and Kiris, C. C., "Fan noise predictions of the NASA source diagnostic test using unsteady simulations with LAVA part I: near-field aerodynamics and turbulence," *AIAA SciTech Forum and Exposition*, 2023.

[8] Fernandes, L. S., Housman, J. A., Stich, G.-D., and Duensing, J. C., "Fan Noise Predictions of the NASA Source Diagnostic Test using Unsteady Simulations with LAVA Part II-Tonal and Broadband Noise Assessment," *30th AIAA/CEAS Aeroacoustics Conference*, 2024.

[9] Brès, G. A., Wang, K., Ivey, C. B., Bose, S., Okubo, G., Kamatsuchi, T., and Tanaka, H., "GPU-Accelerated Large-Eddy Simulations for Aeroacoustic Predictions of a Full-Wheel Multi-Stage Turbofan Engine," *AIAA AVIATION FORUM AND ASCEND 2025*, 2025, p. 3653.

[10] Sinha, S., Cerizza, D., and Schuster, W., "Multiple Pure Tone Noise Predictions of a Propulsion Engine Fan with PowerFLOW," *AIAA AVIATION 2023 Forum*, 2023, p. 4296.

[11] Woodward, R., Hughes, C., Jeracki, R., and Miller, C., "Fan Noise Source Diagnostic Test–Far-field Acoustic Results," *8th AIAA/CEAS Aeroacoustics Conference & Exhibit*, 2002, p. 2427.

[12] Tyler, J. M., and Sofrin, T. G., "Axial flow compressor noise studies," Tech. rep., SAE Technical Paper, 1962.

[13] Peake, N., and Parry, A. B., "Modern challenges facing turbomachinery aeroacoustics," *Annual Review of Fluid Mechanics*, Vol. 44, No. 1, 2012, pp. 227–248.

[14] Hawkings, D., "Multiple tone generation by transonic compressors," *Journal of Sound and Vibration*, Vol. 17, No. 2, 1971, pp. 241–250.

[15] Kurosaka, M., "A note on multiple pure tone noise," *Journal of Sound and Vibration*, Vol. 19, No. 4, 1971, pp. 453–462.

[16] McAlpine, A., and Fisher, M., "On the prediction of "buzz-saw" noise in aero-engine inlet ducts," *Journal of Sound and Vibration*, Vol. 248, No. 1, 2001, pp. 123–149.

[17] Han, F., Sharma, A., Paliath, U., and Shieh, C., "Multiple pure tone noise prediction," *Journal of Sound and Vibration*, Vol. 333, No. 25, 2014, pp. 6942–6959.

[18] Moin, P., Squires, K., Cabot, W., and Lee, S., "A dynamic subgrid-scale model for compressible turbulence and scalar transport," *Physics of Fluids A: Fluid Dynamics*, Vol. 3, No. 11, 1991, pp. 2746–2757.

[19] Lilly, D., "A proposed modification of the Germano subgrid-scale closure method," *Physics of Fluids A*, Vol. 4, No. 3, 1992, pp. 633–635.

[20] Shu, C.-W., and Osher, S., "Efficient implementation of essentially non-oscillatory shock-capturing schemes," *Journal of computational physics*, Vol. 77, No. 2, 1988, pp. 439–471.

[21] Gottlieb, S., Shu, C.-W., and Tadmor, E., "Strong stability-preserving high-order time discretization methods," *SIAM review*, Vol. 43, No. 1, 2001, pp. 89–112.

[22] Wong, M. L., Ghate, A., Kenway, G. K., Angel, J. B., and Kiris, C. C., "Immersed Boundary Wall-Modelled Large Eddy Simulations of Subsonic Jet Flows and Acoustics," *AIAA AVIATION FORUM AND ASCEND 2024*, 2024, p. 4466.

[23] Wong, M. L., Kenway, G. K. W., Ghate, A. S., Angel, J. B., and Kiris, C. C., "Quadcopter Noise Predictions with Wall-Modeled Large Eddy Simulations," 2025.

[24] Wong, M. L., Ghate, A. S., Kenway, G., Angel, J. B., Kiris, E., , and Kiris, C. C., "Counter-Rotating Open Rotor Noise Predictions Using Immersed Boundary Wall-Modeled Large Eddy Simulation," *32nd AIAA/CEAS Aeroacoustics Conference (2026)*, 2026.

[25] Shur, M. L., Spalart, P. R., and Strelets, M. K., "Noise prediction for increasingly complex jets. Part I: Methods and tests," *International journal of aeroacoustics*, Vol. 4, No. 3, 2005, pp. 213–245.

[26] Mendez, S., Shoeybi, M., Lele, S., and Moin, P., "On the use of the Ffowcs Williams-Hawkings equation to predict far-field jet noise from large-eddy simulations," *International Journal of Aeroacoustics*, Vol. 12, No. 1-2, 2013, pp. 1–20.

[27] Kenway, G. K., Ghate, A., Browne, O. M., Wong, M. L., Angel, J. B., and Kiris, C. C., "Immersed Boundary Wall-Modelled Large Eddy Simulations of a Generic Hammerhead Payload Fairing," *AIAA AVIATION FORUM AND ASCEND 2024*, 2024, p. 3693.

[28] Ashton, N., Ghate, A., Kenway, G., Angel, J., Wong, M. L., and Kiris, C. C., "Immersed Boundary Wall-Modelled Large Eddy Simulations for the 5th High-Lift Prediction Workshop," *AIAA SCITECH 2025 Forum*, 2025, p. 0888.

[29] Wong, M. L., Ghate, A., Kenway, G. K., Angel, J. B., and Kiris, C. C., "Immersed Boundary Wall-Modelled Large Eddy Simulations of Straight Wings with Three-Dimensional Ice Accretion," *AIAA AVIATION FORUM AND ASCEND 2024*, 2024, p. 4000.

[30] Angel, J. B., Wong, M. L., Kenway, G., Ghate, A., and Kiris, C. C., "Validation of Immersed Boundary Wall-Modelled Large Eddy Simulations with F-16XL Flight Data," *AIAA AVIATION FORUM AND ASCEND 2024*, 2024, p. 4374.

[31] Angel, J. B., Ghate, A., Kenway, G., Wong, M. L., Kiris, C. C., and Ashton, N., "Immersed boundary wall-modelled large eddy simulations for automotive aerodynamics," *AIAA Aviation Forum and Ascend 2024*, 2024, p. 4172.

[32] Angel, J. B., Ghate, A., Kenway, G., Wong, M. L., and Kiris, C. C., "DLR LK6E2 Missile Airframe Validation Study Using Wall-Modeled Large Eddy Simulations," *AIAA SCITECH 2025 Forum*, 2025, p. 1949.

[33] Ghate, A. S., Angel, J. B., Kenway, G., Wong, M. L., and Kiris, C. C., "Large Eddy Simulations of High-Lift Common Research Model in the NTF Wind Tunnel at Flight Scale Reynolds Numbers," *AIAA SCITECH 2026 Forum*, 2026, p. 0020.

[34] Rahier, G., Prieur, J., Vuillot, F., Lupoglazoff, N., and Biancherin, A., "Investigation of integral surface formulations for acoustic predictions of hot jets starting from unsteady aerodynamic simulations," *9th AIAA/CEAS Aeroacoustics Conference and Exhibit*, 2003, p. 3164.

[35] Mendez, S., Shoeybi, M., Sharma, A., Ham, F., Lele, S., and Moin, P., "Large-eddy simulations of perfectly-expanded supersonic jets: Quality assessment and validation," *48th AIAA Aerospace Sciences Meeting Including the New Horizons Forum and Aerospace Exposition*, 2010, p. 271.

[36] Brès, G. A., Ham, F., Nichols, J. W., and Lele, S. K., "Nozzle wall modeling in unstructured large eddy simulations for hot supersonic jet predictions," *19th AIAA/CEAS Aeroacoustics Conference*, 2013, p. 2142.

[37] Stich, G.-D., Ghate, A. S., Housman, J. A., and Kiris, C. C., "Wall Modeled Large Eddy Simulations for NASA's jet noise consensus database of single-stream, round, convergent jets." *AIAA SCITECH 2022 Forum*, 2022, p. 0684.

[38] Brown, C. A., and Stephens, D. B., "Acoustic Methods Used in the NASA Glenn 9-by 15-Foot Low-Speed Wind Tunnel," Tech. Rep. NASA/TM-2018-218874, 2018.